A hybrid virtual–boundary element formulation for heterogeneous materials

Marco Lo Cascio[a], Alberto Milazzo[a], Ivano Benedetti[a,*]

[a]*Department of Engineering, University of Palermo, Viale delle Scienze, Edificio 8, Palermo, 90128, Italy.*

Abstract

In this work, a hybrid formulation based on the conjoined use of the recently developed virtual element method (VEM) and the boundary element method (BEM) is proposed for the effective computational analysis of multi-region domains, representative of heterogeneous materials. VEM has been recently developed as a generalisation of the finite element method (FEM) and it allows the straightforward employment of elements of general polygonal shape, maintaining a high level of accuracy. For its inherent features, it allows the use of meshes of general topology, including non-convex elements. On the other hand, BEM is an effective technique for the numerical solution of sets of boundary integral equations, employed as the original model of the represented physical problem. For several classes of problems, BEM offers some advantages over more popular techniques, namely the reduction of the dimensionality of the problem, with associated computational savings. In this study, the inherent advantages of VEM and BEM are simultaneously employed for the study of heterogeneous material microstructures.

The method has been applied to *i*) the elastic analysis and *ii*) computational homogenization of fibre-reinforced composite materials and to *iii*) the analysis of composite unit cells exhibiting matrix isotropic damage. The discussed results show how the hybrid technique inherits the generality of VEM and the modelling simplification and accuracy of BEM, ensuring high accuracy and fast convergence and providing a versatile tool for the analysis of multiphase materials, also including non-linear behaviour such as material degradation. Further directions of research are identified and discussed after commenting on the presented results.

Keywords: Fibre-reinforced Composite Materials, Computational Micro-mechanics,

*Corresponding author

Email addresses: marco.locascio01@unipa.it (Marco Lo Cascio), alberto.milazzo@unipa.it (Alberto Milazzo), ivano.benedetti@unipa.it (Ivano Benedetti)

Computational Homogenization, Continuum Damage Mechanics, Virtual Element Method, Boundary Element Method

1. Introduction

In the last few decades, remarkable developments in experimental materials characterisation and a broader availability of high performance computing have contributed to the development of the *materials by design* paradigm [1], which aims at developing novel and sustainable materials with desired optimal features by combining elementary constituents in a bottom-up approach using a variety of production techniques. A pillar of such a paradigm is provided by the capability of *multi-scale materials characterisation and modelling* [2] that, by embodying deeper and richer layers of information about the materials hierarchical organisation, often spanning several different scales, contribute to the understanding of complex material/structural behaviours and to the design of novel high-performance applications, with apparent technological benefits.

In such a context, the possibility of modelling, with acceptable fidelity, the microstructure of a considered material, and the complex interactions between its building blocks, plays a fundamental role. The inclusion of deeper layers of fidelity, however, requires the ability of robustly addressing several kinds of modelling complexities, included those arising, for example, from the need of representing involved material morphological details, which may also present statistical variability. In this respect, the development of computational techniques able to deal with complex and evolving geometries and meshes with accuracy, effectiveness and robustness attracts relevant interest.

In the present work, a hybrid computational technique based on the simultaneous use of the *Virtual Element Method* (VEM) and the *Boundary Element Method* (BEM) is proposed for the computational micro-mechanics and homogenization of heterogeneous materials with complex microstructures, also exhibiting non-linear behaviour, in the form of damage initiation and evolution, in some of the phases.

VEM [3, 4] is a recent and rapidly emerging generalisation of the Finite Element Method (FEM), which allows the use of mesh elements of very general shape, including polygonal elements with an arbitrary number of edges, elements with curved edges [5], non-convex and highly distorted elements, without penalties on the accuracy of the analysis. The method has been successfully applied to a variety of mechanical problems [6, 7, 8, 9, 10, 11, 12, 13], including materials homogenization, see e.g. Refs. [14, 15, 16]. The possibility of using virtual elements of general shape, also highly distorted,

makes them particularly interesting for applications where the meshed domain may undergo large deformations [17] or for problems where the occurrence of problematic morphological features, likely sources of mesh irregularities, may not be *a priori* excluded: a typical example is provided by problems of statistical homogenization, where a relevant number of random unit cells is generated and analysed with the aim of inferring the emerging material properties through volume averaging techniques.

BEM [18, 19] is a numerical strategy based on the use of boundary integral equations for the reformulation of the considered problems: its hallmark is the reduction of the problem dimensionality as a direct consequence of the underlying integral formulation, with ensuing reduction in the number of degrees of freedom required in the analysis, with respect to numerical techniques based on the employment of partial differential equations, either in strong or weak form. The method is know to offer high accuracy at a relatively reduced computational cost, especially in problems requiring accurate representation of the analysis domain boundary. Besides the computational cost savings, the reduction of the model dimensionality generally induces a pre-processing simplification, thanks to the need of discretising curves instead of surfaces, in the 2D case, or surfaces instead of volumes, in the 3D case; such a feature may result particularly appealing when materials morphologies with high statistical variability have to be automatically generated, meshed and analysed [20]. BEM has been successfully employed to the solution of several classes of problems in fluids [21] and solids [19] mechanics and, more recently, in multi-scale materials modelling [22, 23, 24, 25, 26, 27, 28].

The idea put forward in this work is that the conjoined use of VEM and BEM might provide some benefits in the modelling of heterogeneous materials with complex microstructures [29, 30].

While the coupling between FEM and BEM has been explored in the literature [31, 32, 33], to the best of the authors' knowledge, no direct coupling between VEM and BEM has been previously proposed; a FEM-BEM framework and a VEM-VEM framework have been used in Ref.[34], to address the problem of fluid flow in discrete fracture networks, but no direct link between VEM and BEM has been employed.

In the present work, which considers unit cells with stiff inclusions embedded within a more compliant matrix, representative e.g. of the transverse section fibre-reinforced composites, BEM is employed to model the material inclusions, while VEM is used to represent the matrix. This choice is motivated by the assumption that, under progressive loading, the stiffer inclusions remain in the linear behaviour range, while the matrix may undergo complex non-linear phenomena, e.g.

hardening, damaging or fracturing processes, which can be modelled within the framework of VEM, taking advantage of the generality inherited by FEM and its peculiar ability of dealing with elements of very general shapes.

In this contribution, the capabilities of a coupled VEM-BEM approach for computational micromechanics and homogenization of heterogeneous materials with complex microstructures are explored. An isotropic damage VEM model is implemented, to capture the degradation of the matrix in fibre-reinforced composites under progressive loading. The study is organised as follows. Section 2 addresses the generation and meshing strategy for the analysed artificial morphologies. The formulation of the hybrid virtual-boundary element method is described in Section 3, where the features of the lowest-order VEM for elastic problems, Section 3.1, of a VEM formulation for domains exhibiting isotropic damage, Section 3.2, and of BEM for two-dimensional linear elastic problems, Section 3.3, are recalled, before introducing the coupling procedure in Section 3.4. Eventually Section 4 discusses the application of the hybrid procedure to: *i*) a case study represented by a matrix with complex shaped inclusions, assessing the accuracy in terms of displacements and stresses; *ii*) the computational homogenization of a two-phase material with elastic inclusions; *iii*) the analysis of progressive degradation of a composite unit cell consisting of a fibre embedded in epoxy matrix with partial debonding between the two phases. Some concluding remarks are eventually given in the *Conclusions*.

2. Generation and meshing of artificial microstructures

In this Section, the procedures adopted for generating and meshing the artificial representation of the considered material microstructures are described. As it will be shown in Section 3, the present formulation is based on a multi–region approach, in which different phases are modelled using either a *virtual* or a *boundary* element approach, depending on several considerations, including the phase physics, as discussed in Section 5. An example is provided by the unit cell representative of a fibre–reinforced polymer composite, for which a certain number of inclusions, modelled, e.g. with the boundary element method, may represent the transverse section of the fibres, while the surrounding domain, modelled with the virtual element method, may represent the polymer matrix.

In general, the considered two-dimensional unit cell may contain N_V regions modelled with the virtual element method and N_B domains modelled with the boundary element method, so that the

overall domain Ω is given by

$$\Omega = \left(\bigcup_{k=1}^{N_V} \Omega_k^V \right) \cup \left(\bigcup_{k=1}^{N_B} \Omega_k^B \right) = \Omega^V \cup \Omega^B, \tag{1}$$

where the superscripts V and B refer to virtual and boundary element regions respectively. The overall domain is bounded by the contour $\Gamma = \partial\Omega$, while the k–th subdomain Ω_k^B is bounded by the contour $\Gamma_k^B = \partial\Omega_k^B$ and the k–th subdomain Ω_k^V is bounded by the contour $\Gamma_k^V = \partial\Omega_k^V$.

The virtual element regions can be meshed with generic polygonal elements, which ensures certain meshing flexibility, as discussed, e.g. in Ref.[15]. On the other hand, the boundary element regions only require consistent meshes of their contours S_k and do not need any internal mesh, at least when they do not experience any non-linear material process (e.g. plasticity and/or damage). The meshing procedure must then interface the polygonal virtual element mesh with the one–dimensional boundary element mesh. Due to the inherent features of the virtual element method, which allows the natural treatment of generic polygonal elements and hanging nodes, the meshing can be implemented without resorting to complex pre–processing algorithms.

To describe the implemented procedures, the simple example geometry shown in Fig.(1), consisting of a square unit cell with an inclusion of arbitrary shape, is considered. In this case, $\Omega = \Omega^V \cup \Omega^B$ and $\Gamma^B = \partial\Omega^B$ is the interface between the two regions. Once the morphology of the unit cell is geometrically reconstructed, the meshing procedure is based on the generation of a Voronoi tessellation [35] of the overall domain and the subsequent clipping of the internal inclusions to be modelled with BEM.

The workflow of the overall procedure can be summarised as follows:

a) The micro–morphology is created as a two-dimensional geometric entity;

b) A *conformal* triangular mesh of the overall domain is generated;

c) A non-conformal polygonal mesh is generated as the Voronoi dual of the triangular discretisation;

d) The Voronoi cells falling within the inclusion domain are removed;

e) The Voronoi cells intersecting the contour Γ^B are clipped using the nodes and edges of the conformal triangular mesh, thus providing the sought *conformal* polygonal mesh.

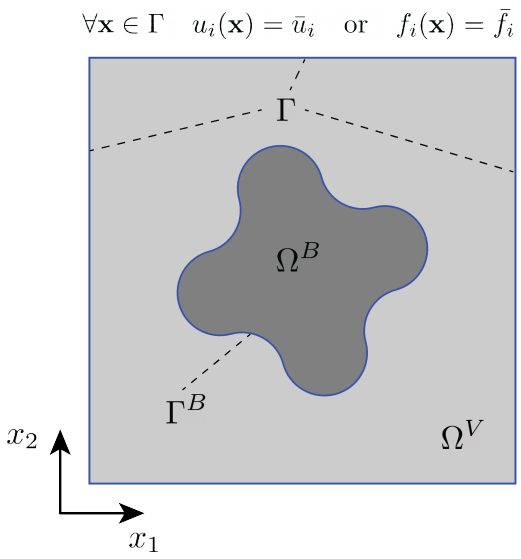

Fig. 1. A microstructure consisting of an arbitrary shaped inclusion within a surrounding matrix as an example two-dimensional heterogeneous unit cell. Boundary conditions are enforced on the boundary $\Gamma = \partial\Omega$ of the microstructure; Γ^B is the interface between Ω^V and Ω^B.

The adjective *conformal* used above refers to the circumstance that the vertices of the initial triangular mesh and those of the target polygonal one lie on the interface S between the two regions, thus identifying the interface mesh nodes, where suitable continuity conditions will be enforced to retrieve the integrity of the domain.

The above procedure, schematically represented in Fig.(2), has been implemented in `MATLAB`. The geometry is represented as a collection of points and curves identifying each subdomain, which forms the input for generating the first conformal triangular mesh of the overall domain. This task has been performed using an unstructured mesh-generator for two-dimensional geometries [36]. The target polygonal mesh is generated from the triangular mesh output using an in–house developed code that performs the following sequence of operations: *a*) retrieves the triangular mesh data structure; *b*) constructs a two-dimensional Voronoi diagram from the given triangulation; *c*) clips the polygonal mesh elements intersecting the interface Γ^B, providing the target conformal polygonal mesh of the domain.

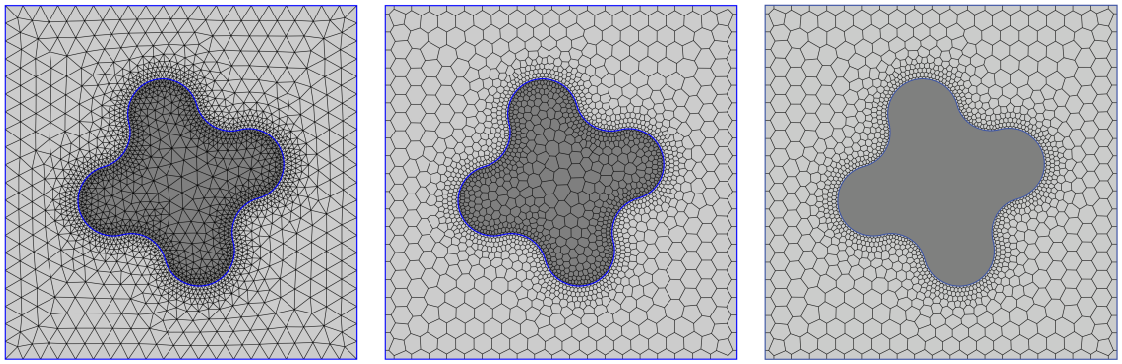

(a) (b) (c)

Fig. 2. Generation of the polygonal mesh of the artificial multi–region morphologies: a) initial conformal triangular mesh of the overall domain; b) two-dimensional Voronoi diagram associated with the previous triangulation; c) target conformal polygonal mesh obtained by removing the Voronoi cells within the inclusion domain and clipping those intersecting the sub–domains interface.

3. The virtual–boundary element formulation

In this work, two–dimensional multi-region morphologies are considered, as described in the previous section. In general, the considered microstructure lyes within the domain Ω and $\mathbf{x} = \{x_1, x_2\}^\intercal \in \Omega$ denotes the coordinates of a generic point within it.

The strong formulation of the small strains elastic problem is based on the use of the strain-displacement equations

$$\varepsilon_{ij}(\boldsymbol{u}) = \frac{1}{2}\left(u_{i,j} + u_{j,i}\right), \tag{2}$$

of the linear elastic constitutive laws

$$\sigma_{ij} = C_{ijkl}\,\varepsilon_{kl}, \tag{3}$$

and of the indefinite equilibrium equations

$$\sigma_{ij,j} + f_i = 0. \tag{4}$$

where $\boldsymbol{u} = \{u_1, u_2\}^\intercal$ represents the displacement vector field, ε_{ij} are the components of the the strain tensor, σ_{ij} are the components of the stress tensor, C_{ijkl} are the stiffness tensor components and f_i are the components of volume distributes loads. Eventually, suitable boundary conditions

are enforced on the boundary $\Gamma \equiv \partial\Omega$ of the the considered body, so that

$$\forall i = 1,2 \quad \begin{cases} u_i = & \bar{u}_i \quad \text{on } \Gamma_{u_i} \\ t_i = & \bar{t}_i \quad \text{on } \Gamma_{t_i} \end{cases} \tag{5}$$

and $\Gamma_{u_i} \cap \Gamma_{t_j} \equiv \emptyset$ if $i = j$ and $\Gamma_{u_i} \cup \Gamma_{t_i} \equiv \Gamma$ for $i = 1, 2$.

It may sometimes be convenient, for the sake of expressivity and compactness, to employ the Voigt notation and express the above sets of equations in matrix form, so that the strain-displacements relationships, the constitutive equations and the equilibrium equations read respectively

$$\boldsymbol{\varepsilon} = \mathscr{D}\boldsymbol{u}, \qquad \boldsymbol{\sigma} = \mathbf{C}\boldsymbol{\varepsilon}, \qquad \mathscr{D}^{\intercal}\boldsymbol{\sigma} + \boldsymbol{f} = \mathbf{0}, \tag{6}$$

with the associated boundary conditions

$$\begin{cases} \boldsymbol{u} = \bar{\boldsymbol{u}} & \text{on } \Gamma_{\boldsymbol{u}} \\ \boldsymbol{t} = \mathscr{D}_n^{\intercal}\boldsymbol{\sigma} = \bar{\boldsymbol{t}} & \text{on } \Gamma_{\boldsymbol{t}} \end{cases} \tag{7}$$

where

$$\mathscr{D} = \begin{bmatrix} \partial_x & 0 \\ 0 & \partial_y \\ \partial_y & \partial_x \end{bmatrix}, \qquad \mathscr{D}_n = \begin{bmatrix} n_x & 0 \\ 0 & n_y \\ n_y & n_x \end{bmatrix} \tag{8}$$

where $\mathscr{D}$ denotes the small-strains linear differential matrix operator, $\partial_x = \partial(\cdot)/\partial x$ and $\partial_y = \partial(\cdot)/\partial y$, n_x and n_y are the components of the boundary unit normal $\boldsymbol{n}$, $\boldsymbol{\sigma} = \{\sigma_1 = \sigma_{11}, \sigma_2 = \sigma_{22}, \sigma_6 = \sigma_{12}\}^{\intercal}$ and $\boldsymbol{\varepsilon} = \{\varepsilon_1 = \varepsilon_{11}, \varepsilon_2 = \varepsilon_{22}, \varepsilon_6 = 2\varepsilon_{12}\}^{\intercal}$.

In this Section the features of both the virtual element and boundary element methods will be described with reference to the above two-dimensional elastic problem. The interface between the two methods will be then formulated and the VE–BE method will eventually be established.

3.1. The virtual element method for elastic domains

The Virtual Element Method may be considered as a generalisation of the Finite Element Method to the treatment of general polygonal or polyhedral mesh elements showing, in this respect, some similarities with other polygonal/polyhedral finite element methods [37].

In VEM, the trial and test functions over a generic polygonal mesh element are selected as the set of all polynomials up to a certain order k *plus* a set of additional functions constituting the

solution of a suitably defined boundary value problem over the considered element. In such an approximation, k identifies the *order* of the virtual element scheme while the auxiliary functions, used in the theoretical derivation of the method, are required to be known only over the element edges; within the element they are neither explicitly known nor computed, thus justifying the label *virtual* attached to the method. Once a weak form of the elastic problem is established, the discrete counterpart of the continuous operators appearing in the variational formulation can be computed by expressing the virtual trial and test functions through their polynomial projections that, through appropriate choice of the element degrees of freedom, can be exactly computed without actually solving the local boundary value problem.

3.1.1. Weak form for 2D linear elasticity

The weak form for the boundary value problem given in Section 3 is provided by the *principle of virtual displacements*, which states that the solution field is given by the displacements $\boldsymbol{u}(\mathbf{x}) \in \mathbf{V}$ satisfying the equality

$$\int_\Omega \boldsymbol{\varepsilon}(\boldsymbol{v})^\intercal \mathbf{C}\, \boldsymbol{\varepsilon}(\boldsymbol{u})\, d\Omega = \int_\Omega \boldsymbol{v}^\intercal \boldsymbol{f}\, d\Omega \qquad \forall \boldsymbol{v}(\mathbf{x}) \in \mathbf{V}, \tag{9}$$

where $\mathbf{V} := \left[H_0^1(\Omega)\right]^2$ is the space of kinematically admissible displacements and $H_0^1(\Omega)$ denotes the first order Sobolev space on Ω, consisting of functions vanishing on Γ and square integrable over Ω together with their first order derivatives. With the sole aim of simplifying the formal introduction of the method, in Eq.(9) it has been assumed that the displacements $\boldsymbol{u}$ vanish along the boundary Γ of the analysed domain. As it will be recalled in Section 3.1.7, the assumption does not affect the generality of the formulation: indeed, due to the choice of the element-wise virtual space of admissible displacements, see Section 3.1.3, either non-homogeneous Dirichlet or Neumann boundary conditions can be implemented following the same procedure as in the standard finite element method[38].

Defining integral operators

$$\mathscr{L}(\boldsymbol{u}, \boldsymbol{v}) := \int_\Omega \boldsymbol{\varepsilon}(\boldsymbol{v})^\intercal \mathbf{C}\, \boldsymbol{\varepsilon}(\boldsymbol{u})\, d\Omega, \qquad \mathscr{G}(\boldsymbol{v}) := \int_\Omega \boldsymbol{v}^\intercal \boldsymbol{f}\, d\Omega, \tag{10}$$

which identify the virtual strain energy symmetric bilinear form and the loads virtual work linear functional, Eq.(9) can be written in the compact form

$$\mathscr{L}(\boldsymbol{u}, \boldsymbol{v}) = \mathscr{G}(\boldsymbol{v}) \quad \forall \boldsymbol{v} \in \mathbf{V}, \tag{11}$$

useful in subsequent developments.

3.1.2. Domain partition and element description

The weak form in Eq.(11) is employed to build an approximate solution to the elastic boundary-value problem. For this purpose, the domain Ω is sub-divided into a set Ω_h of finite non-overlapping elements $E \in \Omega_h$, mutually interconnected at the nodal points lying on their edges. Once the discretisation Ω_h is identified, a function space $\mathbf{V}_h \subset \mathbf{V}$ constituting a finite-dimensional approximation of $\mathbf{V}$ can be associated to it. The Galerkin approximation of the problem is provided by $\boldsymbol{u}_h \in \mathbf{V}_h$ such that

$$\mathscr{L}(\boldsymbol{u}_h, \boldsymbol{v}_h) = \mathscr{G}(\boldsymbol{v}_h) \quad \forall \boldsymbol{v}_h \in \mathbf{V}_h, \tag{12}$$

where the integral operators can be split into elemental contributions $\mathscr{L}_E(\cdot,\cdot)$ and $\mathscr{G}_E(\cdot)$ as

$$\mathscr{L}(\boldsymbol{u}_h, \boldsymbol{v}_h) = \sum_{E\in\Omega_h} \mathscr{L}_E(\boldsymbol{u}_h, \boldsymbol{v}_h) = \sum_{E\in\Omega_h} \int_E \boldsymbol{\varepsilon}(\boldsymbol{v}_h)^{\intercal} \mathbf{C}\, \boldsymbol{\varepsilon}(\boldsymbol{u}_h)\, dE \tag{13}$$

and

$$\mathscr{G}(\boldsymbol{v}_h) = \sum_{E\in\Omega_h} \mathscr{G}_E(\boldsymbol{v}_h) = \sum_{E\in\Omega_h} \int_E \boldsymbol{v}_h^{\intercal} \boldsymbol{f}\, dE. \tag{14}$$

One of the most appealing features of VEM is the possibility of treating polygonal elements with very general shapes: in particular *polygons with an arbitrary number of edges are allowed and even the requirement of convexity may be waived.* For a generic element E, $\mathbf{x}_E = \{x_E, y_E\}$ will denote its centroid, h_E its diameter and $|E|$ its area. The counter-clockwise ordered vertices v_i, $i = 1, 2..., m$, have coordinates $\mathbf{x}_i = \{x_i, y_i\}$ and their *local scaled coordinates* are defined by

$$\xi_i = \frac{x_i - x_E}{h_E}, \qquad \eta_i = \frac{y_i - y_E}{h_E}. \tag{15}$$

The symbol e_i, $i = 1, 2..., m$, will refer to the edge having v_i as its first vertex – see Fig.(3); the element overall boundary will be denoted by ∂E and $\boldsymbol{n}$ is the unit normal vector to ∂E.

3.1.3. Virtual displacements field

In this work the *lowest order* virtual element method is employed to model some regions of the considered microstructures. In the case of the lowest order formulation, i.e. when $k = 1$, the local discrete virtual space of admissible displacements for the generic element E is defined as in Ref.[39], i.e.

$$\begin{aligned} \mathbf{V}_h(E) := \Big\{ \boldsymbol{v}_h \in \left[H^1(E) \cap C^0(E)\right]^2 : \boldsymbol{v}_{h|\partial E} \in \left[C^0(\partial E)\right]^2 ; \\ \boldsymbol{v}_{h|e} \in [P_1(E)]^2 \ \forall e \subset \partial E;\ \mathscr{D}^{\intercal} \mathbf{C}\, \boldsymbol{\varepsilon}(\boldsymbol{v}_h) = \mathbf{0} \text{ in } E \Big\}, \end{aligned} \tag{16}$$

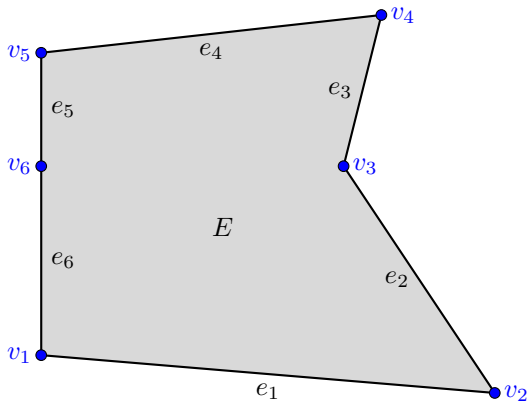

Fig. 3. Example of a non-convex VEM element with hanging nodes.

where the notation $P_k(E)$ indicates the space of polynomials of degree k on E. The global discrete virtual space is thus obtained by

$$\mathbf{V}_h := \left\{ \boldsymbol{v}_h \in \mathbf{V} : \boldsymbol{v}_{h|E} \in \mathbf{V}_h(E) \quad \forall E \in \Omega_h \right\}. \tag{17}$$

Differently from classical FEM, $\boldsymbol{v}_h \in \mathbf{V}_h(E)$ are explicitly known only on ∂E and their explicit knowledge is not required over the whole element domain, thus justifying, as mentioned, the label *virtual*. For the case $k = 1$:

- The degrees of freedom associated with E are the point-wise values of $\boldsymbol{v}_h$ at its vertices v_i;
- The functional components of $\boldsymbol{v}_h$ are linear polynomials along each edge $e_i \subset \partial E$ and they are globally continuous on ∂E.

The choice of the lowest order formulation is motivated, besides its simplicity and ease of implementation, by the fact it ensures a straightforward coupling with the boundary element equations employed for modelling the microstructural inclusions, see Section 3.4, which are based on a linear approximation of the displacements and traction fields along each boundary element. However, higher order virtual element formulations have been proposed in the literature. Their possible use within the present framework is briefly discussed in Section 5, but their in-depth treatment go beyond the scope of the present contribution. The interested readers are referred to Refs.[40, 39, 4] for further details.

3.1.4. Elemental projector operator

Being the components of $\boldsymbol{v}_h$ not explicitly available, the local discrete bilinear form $\mathscr{L}_E(\cdot,\cdot)$ cannot be computed by standard numerical integration, as classically done in FEM. For this purpose, VEM employs a *projector* operator Π, defined on E by the orthogonality condition

$$\int_E \boldsymbol{p}^{\mathsf{T}} \left[\Pi(\boldsymbol{v}_h) - \boldsymbol{\varepsilon}(\boldsymbol{v}_h)\right] dE = 0 \quad \forall \boldsymbol{p} \in \left[P_0(E)\right]^3, \tag{18}$$

which identifies $\Pi(\boldsymbol{v}_h)$ as an *approximation* of the strains field associated to the *unknown* displacements $\boldsymbol{v}_h$, so that the error with respect to the approximated field has no components along the space of polynomial of order $k-1$ over E. Having $\boldsymbol{p}$ constant components when $k=1$, Eq.(18) yields

$$\Pi(\boldsymbol{v}_h) = \frac{1}{|E|} \int_E \boldsymbol{\varepsilon}(\boldsymbol{v}_h)\, dE. \tag{19}$$

The projector operator and its discrete counterpart have a key role in VEM.

3.1.5. Projector operator matrix

To be effectively employed, the projector operator must be computed in a discrete form. To do so, each function $\boldsymbol{v}_h \in \mathbf{V}_h(E)$, whose explicit expression is unknown, can be thought as

$$\boldsymbol{v}_h = \mathbf{N}\left(\xi,\eta\right)\, \tilde{\boldsymbol{v}} \tag{20}$$

where $\tilde{\boldsymbol{v}} = [\tilde{v}_{x1},\, \tilde{v}_{y1},\, \ldots,\, \tilde{v}_{xm},\, \tilde{v}_{ym}]^{\mathsf{T}}$ collects the point-wise values of $\boldsymbol{v}_h$ associated with the element vertices and $\mathbf{N}\left(\xi,\eta\right) \in \mathbb{R}^{2\times 2m}$ collects the *virtual* shape functions $N_i(\xi,\eta)$, never explicitly represented within the element domain, associated with each vertex i of the element E, analogously to what is done in the standard FEM. It is important to realise that the functional entries of the matrix $\mathbf{N}\left(\xi,\eta\right)$ are never analytically known at the interior points of the generic element; only their restriction to the element edges is explicitly known, due to the features of the space $\mathbf{V}_h(E)$ defined in Section 3.1.3. Here, along the lines of Ref.[38], the expression in Eq.(20) is introduced to allow a formal presentation of the method more suited to readers with an engineering background, thus familiar with the concept of shape functions.

Employing Eq.(20) in Eq.(19), and considering the strain-displacement relationship in Eq.(6), yields

$$\Pi(\boldsymbol{v}_h) = \frac{1}{|E|} \int_E \mathscr{D}\left(\mathbf{N}\tilde{\boldsymbol{v}}\right) dE = \frac{1}{|E|} \left(\int_{\partial E} \mathscr{D}_n \cdot \mathbf{N}\, d\partial E \right) \tilde{\boldsymbol{v}} = \boldsymbol{\Pi}\, \tilde{\boldsymbol{v}}, \tag{21}$$

where the boundary integral appearing in the third term has been obtained applying the Green's theorem to the domain integral and the operator $\mathscr{D}_n$ has been defined in Eq.(8).

Eq.(21) defines the discrete projector operator $\mathbf{\Pi} \in \mathbb{R}^{3\times 2m}$ as

$$\mathbf{\Pi} = \frac{1}{|E|}\int_{\partial E} \mathscr{D}_n \cdot \mathbf{N}\, d\partial E = \frac{1}{|E|}\sum_{k=1}^{m}\int_{e_k} \mathscr{D}_n \cdot \mathbf{N}\, ds, \tag{22}$$

which *can now be explicitly computed*, as the restriction of the shape functions $N_i(\xi,\eta)$ to the element edges e_k are *known* piece-wise linear polynomials.

On each virtual element, the (constant) approximated strain field $\boldsymbol{\varepsilon}_\Pi$ can be computed using the local projector matrix $\mathbf{\Pi}$ and the nodal values of the displacement components $\tilde{\boldsymbol{v}}$

$$\boldsymbol{\varepsilon}_\Pi = \mathbf{\Pi}\,\tilde{\boldsymbol{v}} \tag{23}$$

3.1.6. Virtual element stiffness matrix

Once the local projector has been defined, the local symmetric bilinear form $\mathscr{L}_E(\cdot,\cdot)$ appearing in Eq.(13) can be expressed as

$$\mathscr{L}_{E,h}(\boldsymbol{u}_h,\boldsymbol{v}_h) = \int_E \Pi(\boldsymbol{v}_h)^\intercal \mathbf{C}\,\Pi(\boldsymbol{u}_h)\, dE + s_E(\boldsymbol{u}_h,\boldsymbol{v}_h), \tag{24}$$

where the terms on the right hand side identify the so-called *consistency* and *stability* terms [40], respectively. As it will be shown, upon discretisation

$$\mathscr{L}_{E,h}(\boldsymbol{u}_h,\boldsymbol{v}_h) = \tilde{\boldsymbol{v}}^\intercal\, \mathbf{K}_E\, \tilde{\boldsymbol{u}}, \tag{25}$$

which defines is the element *virtual stiffness matrix*

$$\mathbf{K}_E = \mathbf{K}_E^c + \mathbf{K}_E^s, \tag{26}$$

stemming as the sum of the consistency and stability terms $\mathbf{K}_E^c,\ \mathbf{K}_E^s \in \mathbb{R}^{2m\times 2m}$.

The consistency term ensures that, if the solution of the original problem is globally a linear polynomial, then the discrete solution and the exact solution coincide. Using the virtual element approximation in Eq.(21), such a term can be approximated as

$$\int_E \Pi(\boldsymbol{v}_h)^\intercal \mathbf{C}\,\Pi(\boldsymbol{u}_h)\, dE = \tilde{\boldsymbol{v}}^\intercal \left(\int_E \mathbf{\Pi}^\intercal\, \mathbf{C}\, \mathbf{\Pi}\, dE\right) \tilde{\boldsymbol{u}} = \tilde{\boldsymbol{v}}^\intercal\, \mathbf{K}_E^c\, \tilde{\boldsymbol{u}} \tag{27}$$

which, being the integrand constant over E, readily gives

$$\mathbf{K}_E^c = |E|\, \mathbf{\Pi}^\intercal \mathbf{C}\, \mathbf{\Pi}. \tag{28}$$

The stability term, on the other hand, is a symmetric bilinear form that ensures proper rank to $\mathbf{K}_E$ and it may be written as

$$s_E\left(\boldsymbol{u}_h, \boldsymbol{v}_h\right) = \tilde{\boldsymbol{v}}^{\intercal}\, \mathbf{K}_E^s\, \tilde{\boldsymbol{u}}. \tag{29}$$

Following Ref.[38], the matrix stability contribution can be computed as

$$\mathbf{K}_E^s = \left(\mathbf{I} - \mathbf{\Pi}^s\right)^{\intercal} \mu\, \left(\mathbf{I} - \mathbf{\Pi}^s\right), \tag{30}$$

where $\mathbf{I} \in \mathbb{R}^{2m \times 2m}$ is the identity matrix, $\mathbf{\Pi}^s$ is the matrix projector operator

$$\mathbf{\Pi}^s = \mathbf{D}\left(\mathbf{D}^{\intercal}\mathbf{D}\right)^{-1} \mathbf{D}^{\intercal} \tag{31}$$

with

$$\mathbf{D} = \begin{bmatrix} 1 & 0 & \xi_1 & 0 & \eta_1 & 0 \\ 0 & 1 & 0 & \xi_1 & 0 & \eta_1 \\ \vdots & \vdots & \vdots & \vdots & \vdots & \vdots \\ 1 & 0 & \xi_m & 0 & \eta_m & 0 \\ 0 & 1 & 0 & \xi_m & 0 & \eta_m \end{bmatrix} \tag{32}$$

and ξ_i and η_i are the local scaled coordinates of the element vertices defined in Eq.(15). Eventually, as discussed in Ref.[39], $\mu = \tau \operatorname{tr}\left(\mathbf{K}_E^c\right)$ is a constant parameter used to ensure the correct scaling of the stability term with respect to the element size and material constants and, for linear elasticity problems, the value $\tau = 0.5$ can be selected.

3.1.7. Loading vectors

Eventually, for the lowest order VEM, following Ref.[40] the local contribution $\mathscr{G}_E(\cdot)$ to the virtual work of the volume load $\boldsymbol{f}$ appearing at the right-hand side of Eq.(12), if existing, can be approximated as

$$\mathscr{G}_E\left(\boldsymbol{v}_h\right) \approx \mathscr{G}_{h,E}\left(\boldsymbol{v}_h\right) = \int_E \bar{\boldsymbol{v}}_h^{\intercal} \boldsymbol{f}_h \, dE \tag{33}$$

where

$$\bar{\boldsymbol{v}}_h = \frac{1}{m} \sum_{i=1}^{m} \boldsymbol{v}_h(\tilde{\boldsymbol{x}}_i) = \frac{1}{m} \sum_{i=1}^{m} \mathbf{N}(\tilde{\boldsymbol{x}}_i)\tilde{\boldsymbol{v}} \tag{34}$$

denotes the average value of $\boldsymbol{v}_h$ at the vertices of E and

$$\boldsymbol{f}_h = \Pi_0\left(\boldsymbol{f}\right) := \frac{1}{|E|} \int_E \boldsymbol{f} \, dE. \tag{35}$$

is the $L^2(E)$ projection onto constants of the load $\boldsymbol{f}$.

On the other hand, in the case of distributed tractions $\boldsymbol{t}(\boldsymbol{x})$, acting along the edge e_k of the generic virtual element E, i.e. $\forall \boldsymbol{x} \in e_k \subset \partial E$, the knowledge of the explicit expression of the restrictions of the shape functions N_i to the element edges allows the computation of the virtual work of tractions and the convenient definition of nodal forces in terms of nodal values of tractions, which makes the coupling between contiguous virtual element and boundary element domains straightforward, as it will be shown in Section 3.4. Eventually, it is worth noting that, since the shape functions N_i are explicitly known on the element edges, non-homogeneous boundary conditions over the virtual elements can be enforced exactly as in standard FEM.

Denoting with $\tilde{\boldsymbol{f}}$ the nodal forces, which in general include volume end edge contributions, and considering the definition of stiffness matrix given in Eq.(26), it is possible to write the elemental equilibrium equations of elasticity within the framework of the lowest-order VEM as

$$\mathbf{K}_E \, \tilde{\boldsymbol{u}} = \tilde{\boldsymbol{f}}. \tag{36}$$

Once the elemental matrices are computed, the overall structural problem can be addressed employing standard FE numbering, assembly and solution procedures, which motivates the appeal of VEM as a versatile method requiring minimum re-coding in existing software packages. The discrete equations for the overall VE domain can be written

$$\mathbf{K}^{\mathrm{V}} \mathbf{U}^{\mathrm{V}} = \mathbf{F}^{\mathrm{V}} \tag{37}$$

where the superscript V is employed to identify terms stemming from the virtual element model and differentiate them from those associated with the boundary element model of the inclusions.

3.2. The virtual element method for domains exhibiting isotropic damage

In this section, a VEM formulation for modelling regions exhibiting isotropic damage is described. The formulation is based on the employment of the concepts of *continuum damage mechanics*[41, 42, 43], which offers the tools to describe the progressive loss of material integrity due to the propagation and coalescence of microscopic defects, which lead to irreversible material degradation and loss of stiffness observed at the macroscopic scale.

Different approaches have been used to model the growth and effects of distributed microscopic defects at the macroscopic scale. The *isotropic damage model* [44, 45, 46, 47] adopted herein is based

on the simplifying assumption that the loss of material integrity is caused by an equal degradation of the bulk and shear moduli and it is governed by a single internal scalar *damage variable* ω, which is used to track and measure the loss of stiffness of the material. The damage value grows monotonically within its admissible range $0 \leq \omega \leq 1$, where 0 represents the pristine material and 1 a fully degraded material. Under such assumptions, the constitutive equations for an isotropic damage model are defined by [48]

$$\boldsymbol{\sigma} = (1-\omega)\,\mathbf{C}^0\,\boldsymbol{\varepsilon} = (1-\omega)\tilde{\boldsymbol{\sigma}}, \tag{38}$$

where, in Voigt notation, $\boldsymbol{\sigma}$ and $\boldsymbol{\varepsilon}$ collect, respectively, the stress and strain components, $\mathbf{C}^0$ is the elasticity matrix for the pristine elastic material, and $\tilde{\boldsymbol{\sigma}}$ represents the stress components that would be associated to the strains $\boldsymbol{\varepsilon}$ in the undamaged material.

The evolution of damage is triggered upon fulfilment of the activation threshold condition

$$F(\boldsymbol{\varepsilon}) = \tau(\boldsymbol{\varepsilon}) - r = 0, \qquad r = \max_{\lambda \in \mathcal{H}} \{\tau(\lambda)\} \tag{39}$$

where $\tau(\boldsymbol{\varepsilon})$ is a suitably chosen norm of the strains, used to determine if the considered stress state belongs to the elastic domain, when $F(\boldsymbol{\varepsilon}) < 0$, or if it induces damage initiation or evolution, $F(\boldsymbol{\varepsilon}) = 0$, and the monotonically increasing internal variable r represents the damage threshold at the current loading step λ and it is a function of the loading history $\mathcal{H}$. Different choices for the threshold function $\tau(\boldsymbol{\varepsilon})$ are available in the literature, defining different shapes of the elastic domain in the strains space. An expression proposed by Mazars [49] and frequently used in the modelling of quasi-brittle materials, e.g. concrete, defines $\tau(\boldsymbol{\varepsilon})$ as

$$\tau(\boldsymbol{\varepsilon}) = \sqrt{\sum_{i}^{3} \langle \varepsilon_i \rangle^2}, \tag{40}$$

where ε_i are the principal strains and $\langle \cdot \rangle$ are the Macaulay brackets such that $\langle \varepsilon_i \rangle = (\varepsilon_i + |\varepsilon_i|)/2$. To model the onset and evolution of damage in epoxy resins, often used as matrix in fibre-reinforced composite materials, which exhibit different behaviour in tension and compression, Melro et al.[50] proposed the following law

$$\tau(\boldsymbol{\varepsilon}) = \frac{3\tilde{J}_2}{X_m^c X_m^t} + \frac{\tilde{I}_1 (X_m^c - X_m^t)}{X_m^c X_m^t}, \tag{41}$$

where X_m^t and X_m^c are, respectively, the tensile and compressive strengths of the epoxy resin and $\tilde{I}_1$ and $\tilde{J}_2$ are, respectively, the first stress invariant and the second deviatoric stress invariant;

both quantities are defined using the effective stress components $\tilde{\boldsymbol{\sigma}}$ that would be active in the undamaged material.

The evolution of damage is governed by the Kuhn-Tucker flow rules, which read

$$F \leq 0, \quad \dot{r} \geq 0, \quad \dot{r}\, F = 0, \tag{42}$$

and allow to distinguish between loading and unloading conditions. Unloading occurs when $\dot{\tau} \leq 0$; otherwise, damage evolves and the following consistency condition must be satisfied

$$\dot{F} = \dot{\tau} - \dot{r} = 0. \tag{43}$$

The damage evolution law defines the evolution of the damage ω after its onset. An exponential softening can be modelled by adopting a damage law defined as in Ref.[51] as

$$\omega(r) = \left[1 - \frac{r_0}{r} \exp\left(-\frac{r - r_0}{r_f - r_0}\right)\right] \cdot H\left(r - r_0\right), \qquad r = \max_{\lambda \in \mathcal{H}} \left\{\tau(\lambda)\right\} \tag{44}$$

where $H\left(\cdot\right)$ denotes the Heaviside step function, the parameter r_0 identifies the damage initiation condition and r_f specifies the softening response behaviour.

The VEM formulation described in Section 3 can be readily extended to problems involving nonlinear material behaviours such as degradation and damage evolution, as described in Refs.[52, 53]. As in nonlinear finite element formulations, the nonlinear constitutive laws appearing in Eq.(38) can be treated using standard incremental-iterative algorithms. The stress at a generic point $\boldsymbol{x}$ and at a generic loading step λ is given by the expression

$$\boldsymbol{\sigma} = \boldsymbol{\sigma}(\lambda, \boldsymbol{x}, \boldsymbol{\varepsilon}_{\Pi}, \mathcal{H}), \tag{45}$$

where $\boldsymbol{\varepsilon}_{\Pi}$ is the approximated virtual strain computed as in Eq.(23), using the matrix projector operator $\mathbf{\Pi}$. The tangent material stiffness matrix $\mathbf{C}_{tan}$ is consistently computed from the constitutive law in Eq.(45) as

$$\mathbf{C}_{tan}(t, \boldsymbol{x}, \boldsymbol{\varepsilon}_{\Pi}, \mathcal{H}) = \frac{\partial \boldsymbol{\sigma}}{\partial \boldsymbol{\varepsilon}_{\Pi}}. \tag{46}$$

A pure lowest-order VE formulation has already been applied for modelling the strain-softening response of concrete-like materials [11]. In the present work, the non-linear VE formulation will be employed to model the degradation and damage evolution of the matrix phase of unidirectional fibre-reinforced composite materials, while the fibres will be modelled resorting to BEM, in the proposed hybrid framework.

3.2.1. Integral-type non-local regularisation

In the previous Section, the essential features of isotropic damage modelling have been recalled. Although the formulation is straightforward to implement, the direct application of the above damage model may lead to pathological mesh dependency, due to the occurrence of damage *localisation*. To avoid such issues and restore mesh objectivity, continuum damage models require suitable regularisation techniques. *Integral-type non-local* formulations are effective and frequently used regularisation techniques based on the assumption that damage at a point $\boldsymbol{x}$ depends on mechanical quantities suitably averaged over a region surrounding the point $\boldsymbol{x}$ itself [54, 55, 56, 57, 58]. Different non-local models have been proposed, see e.g. Ref.[55], differing for the selected averaged variable.

The non-local approach employed here consists in replacing the local value of the equivalent strain $\tau(\boldsymbol{x})$ with its weighted average $\bar{\tau}(\boldsymbol{x})$ defined as

$$\bar{\tau}(\boldsymbol{x}) = \int_{\Omega} \alpha(\boldsymbol{x}, \boldsymbol{y}) \tau(\boldsymbol{y}) \, d\Omega\,(\boldsymbol{y})\,, \tag{47}$$

where Ω is the analysis domain. Eq.(47) embodies the assumption that strains (and stresses) at a certain point depend, not only on the state variables at that point, but also on the distribution of the state variables over the whole body, or at least over a finite neighbourhood of the point under consideration. The non-local weight function α must satisfy the normalisation condition

$$\int_{\Omega} \alpha(\boldsymbol{x}, \boldsymbol{y}) \, d\Omega\,(\boldsymbol{y}) = 1 \quad \forall \boldsymbol{x} \in \Omega. \tag{48}$$

This may be achieved by adopting the following scaled expression

$$\alpha(\boldsymbol{x}, \boldsymbol{y}) = \frac{\alpha_0\,(\boldsymbol{x}, \boldsymbol{y})}{\int_{\Omega} \alpha_0\,(\boldsymbol{x}, \boldsymbol{y}) \, d\Omega\,(\boldsymbol{y})}, \tag{49}$$

where $\alpha_0\,(\boldsymbol{x}, \boldsymbol{y}) = \alpha_0\,(d)$ is a non-negative weight function usually expressed in terms of the distance $d = ||\boldsymbol{x} - \boldsymbol{y}||$ between two considered material points, monotonically decreasing for $d \geq 0$. The weight function α_0 is often chosen as the truncated quadratic polynomial function

$$\alpha_0\,(d) = \left\langle 1 - \frac{d^2}{R^2} \right\rangle^2, \tag{50}$$

where R is known as the *interaction radius* and it is a parameter related to the *internal* or *characteristic length* l_c of the non-local continuum, which depend on the heterogenous material features [55].

It is worth noting that for the non-local model to be effective, the size of the mesh elements within the zone where the damage process occurs must be smaller than the interaction radius R. In the lowest-order VEM formulation, the computed strain field is constant over a generic mesh element, and no integration weight actually exist. The approach adopted here consist in considering the centroid of each element as the evaluation point and the corresponding weight is taken as the area of the considered element.

3.3. The boundary element method

Differently from finite element methods, the starting point for any boundary element formulation of a physical or engineering problem, is the expression of its governing laws in terms of integral equations. For linear problems, such integral formulations can be built by exploiting the superposition principle and the knowledge of the problem's Green's functions, see e.g. Refs.[59, 60, 19].

For linear elastic problems, considering a generic BEM subdomain Ω^B with boundary Γ^B, in absence of body forces, the *displacements boundary integral equation* [59] can be written

$$c_{ij}\left(\boldsymbol{x}_0\right)\, u_j\left(\boldsymbol{x}_0\right) + \int_{\Gamma^B} H_{ij}\left(\boldsymbol{x}_0, \boldsymbol{x}\right)\, u_j\left(\boldsymbol{x}\right) d\Gamma = \int_{\Gamma^B} G_{ij}\left(\boldsymbol{x}_0, \boldsymbol{x}\right)\, t_j\left(\boldsymbol{x}\right) d\Gamma \tag{51}$$

where $i, j = 1, 2$, $\boldsymbol{x}_0 \in \Gamma^B$ is a generic boundary *collocation* point, $\boldsymbol{x} \in \Gamma^B$ is a generic boundary *integration* point, $u_i(\boldsymbol{x})$ and $t_i(\boldsymbol{x})$ are displacement and traction components at the point $\boldsymbol{x} \in \Gamma^B$, c_{ij} are free terms depending on the geometry of the boundary at the point $\boldsymbol{x}_0$. The kernels $H_{ij}(\boldsymbol{x}_0, \boldsymbol{x})$ and $G_{ij}(\boldsymbol{x}_0, \boldsymbol{x})$ are the *known* components of the fundamental solutions whose analytic expression for 2D elastic problems may be found e.g. in Refs.[60, 19]. It is worth noting that Eq.(51) holds also for anisotropic inclusions, as long as anisotropic fundamental solutions are employed.

The numerical solution of Eq.(51) is based on the discretisation of Γ^B and the subsequent approximation of the boundary displacement and traction components in terms of shape functions and nodal values. More specifically, Γ^B is subdivided into m straight segments s_k and two nodes are associated with the ends of each segment. In plane problems, each node carries two components of displacements and two components of tractions. Assuming Γ^B as smooth, it follows that a tangent can be associated to any $\boldsymbol{x} \in \Gamma^B$, so that the existence of a unique value of traction at the node is ensured; corner points are not considered in the present formulation, although these could be treated resorting to known boundary element techniques [19].

Displacement and traction components are here assumed to be globally continuous over Γ^B and

to vary linearly over each boundary element s_k according to

$$\boldsymbol{u}(\zeta) = \mathbf{N}(\zeta)\ \tilde{\boldsymbol{u}}^k, \qquad \boldsymbol{t}(\zeta) = \mathbf{N}(\zeta)\ \tilde{\boldsymbol{t}}^k \tag{52}$$

where the vectors $\boldsymbol{u}(\zeta)$ and $\boldsymbol{t}(\zeta)$ collect the components of displacements and points belonging to the segment s_k, the matrix $\mathbf{N}(\zeta) \in \mathbb{R}^{2\times 4}$ collects the 1D linear shape functions for the boundary segment s_k, expressed as function of the natural coordinate ζ and $\tilde{\boldsymbol{u}}^k, \tilde{\boldsymbol{t}}^k \in \mathbb{R}^{4\times 1}$ collect the nodal components of displacements and tractions associated with the two ends of the boundary element s_k. It is worth noting that the shape functions $N(\zeta)$, used for the boundary element modelling of the inclusions, could be seen as restrictions over the element edges of the shape functions $N(\xi,\eta)$ appearing in Eq.(20), used in the approximation of the virtual elements fields. Indeed, in the case of the lowest order VEM, the restriction of the shape functions over the edges of a polygonal virtual element is linear, which ensures consistency at the interface between matrix (VEM) and inclusions (BEM).

Writing Eq.(51) for the generic boundary node p and $i = 1, 2$ in matrix form gives

$$\mathbf{c}\,\tilde{\boldsymbol{u}}_p + \sum_{q=1}^{m}\left[\int_{s_q} \mathbf{H}_{pq}(\zeta)\,\mathbf{N}(\zeta)J(\zeta)\,d\zeta\right]\tilde{\boldsymbol{u}}^q = \sum_{q=1}^{m}\left[\int_{s_q} \mathbf{G}_{pq}(\zeta)\,\mathbf{N}(\zeta)J(\zeta)\,d\zeta\right]\tilde{\boldsymbol{t}}^q \tag{53}$$

where $\mathbf{c} \in \mathbb{R}^{2\times 2}$ depends on the geometry of the boundary at the considered collocation point p, smooth in this case, $\tilde{\boldsymbol{u}}_p \in \mathbb{R}^{2\times 1}$ collects the components of displacements at the node p, $\mathbf{H}_{pq}(\zeta), \mathbf{G}_{pq}(\zeta)$ collect the components of the fundamental solution, when the integral equations are collocated at the node p and integrated over the element q, $\tilde{\boldsymbol{u}}^q, \tilde{\boldsymbol{t}}^q \in \mathbb{R}^{4\times 1}$ collect the nodal displacements and tractions associated with the ends of the generic boundary element s_q, according to Eq.(52), and $J(\zeta)$ is the Jacobian of the transformation between segment local and natural coordinates. After numerical integration, Eq.(53) may be rewritten in compact form as

$$\mathbf{H}_p\mathbf{U}^{\mathrm{B}} = \mathbf{G}_p\mathbf{T}^{\mathrm{B}} \tag{54}$$

where $\mathbf{H}_p, \mathbf{G}_p \in \mathbb{R}^{2\times 2m}$ denote the rectangular matrices obtained by collocating at the node p and integrating over the whole boundary Γ^B, while $\mathbf{U}^{\mathrm{B}}, \mathbf{T}^{\mathrm{B}} \in \mathbb{R}^{2m\times 1}$ collect the components of displacements and tractions for all the nodes identified on Γ^B, with the superscript B introduced to highlight that such quantities are associated with the BEM domain. Writing Eq.(54) $\forall p \in [1, ..., m]$ produces the set of linear algebraic equations

$$\mathbf{H}\,\mathbf{U}^{\mathrm{B}} = \mathbf{G}\,\mathbf{T}^{\mathrm{B}}, \tag{55}$$

where $\mathbf{H}, \mathbf{G} \in \mathbb{R}^{2m \times 2m}$ collect matrix blocks of the form appearing in Eq.(54). It is worth noting that, when the BEM domain identifies an inclusion in the analysed domain, both $\mathbf{U}^{\mathrm{B}}$ and $\mathbf{T}^{\mathrm{B}}$ are unknown quantities that must be determined by interfacing Eq.(55) with the equations produced by the model employed for the matrix domain.

3.3.1. Computation of displacements and stresses within BEM domains

Once the displacements and tractions at the boundary of the inclusions modelled with BEM are known, e.g. from the solution of the coupled VE-BE scheme, the value of displacements and stresses at points *within* the inclusions may be computed in post-processing.

Interior points displacements may be computed employing the boundary integral representation

$$u_j\left(\boldsymbol{x}_0\right) + \int_{\Gamma^B} H_{ij}\left(\boldsymbol{x}_0, \boldsymbol{x}\right)\, u_j\left(\boldsymbol{x}\right) d\Gamma = \int_{\Gamma^B} G_{ij}\left(\boldsymbol{x}_0, \boldsymbol{x}\right)\, t_j\left(\boldsymbol{x}\right) d\Gamma, \tag{56}$$

which differs from Eq.(51) for the absence of the coefficients $c_{ij}\left(\boldsymbol{x}_0\right)$, arising from the limiting boundary collocation process.

Internal stresses, on the other hand, may be computed from the boundary integral representation

$$\sigma_{ij}\left(\boldsymbol{x}_0\right) + \int_{\Gamma^B} S_{ijk}\left(\boldsymbol{x}_0, \boldsymbol{x}\right)\, u_k\left(\boldsymbol{x}\right) d\Gamma = \int_{\Gamma^B} D_{ijk}\left(\boldsymbol{x}_0, \boldsymbol{x}\right)\, t_k\left(\boldsymbol{x}\right) d\Gamma, \tag{57}$$

obtained by differentiating Eq.(56), to obtain the integral representation of strains at the considered interior point, and then using the constitutive equations, see e.g. Refs.[60, 19].

Eqs.(56-57) express displacements and stresses at internal points as a function of known displacements and tractions at points along the boundary of the inclusion. The numerical integration of such equations is generally straightforward, except for internal points whose distance from the boundary is less than the size of the employed boundary elements. In such cases, the integrals appearing in Eqs.(56-57) become *nearly singular*, as the distance $r\left(\boldsymbol{x}_0, \boldsymbol{x}\right)$ between the collocation and integration points appears at the denominator of the kernels H_{ij}, G_{ij}, S_{ijk}, D_{ijk}. In such cases, specific integration schemes may be employed to enhance the accuracy of the integration, see e.g. Refs.[61, 62]. In the present work, a simple technique has been implemented: *i*) internal points are selected so that their distance from the boundary is no less than half the boundary element length; *ii*) the order of the Gauss quadrature over the elements closer to the selected point is increased with respect to the order of integration employed for the far elements. The accuracy of the method has been assessed in simple benchmark tests and the absence of artefacts has been verified in the

analysed test cases. However, the technique is not general and the use of specific schemes for nearly singular integrals should be considered in general implementations [19, 61, 62].

For further details about the use of Eqs.(56-57) and their numerical treatments, the interested readers are referred to Refs.[60, 19].

3.4. Continuity conditions at the interface between VE and BE domains

The coupling between boundary and finite elements has been achieved in the literature using various approaches [31, 63, 64, 32, 33]. In this work, to couple the virtual and the boundary element equations, the BEM subdomains are treated as a macro-finite elements and the *traction*-displacement equations associated with them are transformed into *force*-displacement equations and assembled with the VE equations, already expressed in terms of nodal forces and displacements.

The vectors $\mathbf{U}^{\mathrm{V}}$ and $\mathbf{F}^{\mathrm{V}}$ appearing in Eq.(37) collect the nodal components of displacements and forces of all the VEM nodes in the considered domain. Since only some of such nodes belong to the interface Γ^B between boundary and virtual elements, it is possible to partition the vectors as

$$\mathbf{U}^{\mathrm{V}} = \begin{bmatrix} \mathbf{U}_\Gamma \\ \mathbf{U}_\Omega \end{bmatrix}^{\mathrm{V}}, \qquad \mathbf{F}^{\mathrm{V}} = \begin{bmatrix} \mathbf{F}_\Gamma \\ \mathbf{F}_\Omega \end{bmatrix}^{\mathrm{V}}, \tag{58}$$

where $\mathbf{U}^{\mathrm{V}}_\Gamma$ and $\mathbf{F}^{\mathrm{V}}_\Gamma$ identify components related to nodes belonging to Γ^B. Along such interfaces, the nodal displacements and forces must satisfy the compatibility and equilibrium conditions

$$\mathbf{U}^{\mathrm{B}} = \mathbf{U}^{\mathrm{V}}_\Gamma, \qquad \mathbf{F}^{\mathrm{B}} + \mathbf{F}^{\mathrm{V}}_\Gamma = \mathbf{0}, \tag{59}$$

which have been written considering that no external nodal forces act on the nodes belonging to Γ^B. The displacement continuity equations can be readily written, as the displacement components appearing in the VEM system (37) and in the BEM system (55) carry the same physical meaning. On the contrary, while nodal *forces* appear in Eq.(37), related to the VEM domain, nodal components of *tractions* appear in Eq.(55), related to the BEM domain, so that it is necessary to retrieve a consistent expression of the nodal forces associated to the BEM tractions, before writing the equilibrium equations appearing in Eq.(59).

For a generic boundary element node this can be accomplished by resorting to appropriate energy considerations. In the scheme adopted in this work, since two-node piecewise linear continuous boundary elements are used, a generic node always lies at the conjunction between two contiguous

boundary elements. It is here recalled that, in the considered 2D background, boundary elements are 1D segments, which are interfaced with the *edges* of the 2D virtual elements. If the generic node i lies between the boundary elements s_k and s_{k+1}, then, for a virtual displacement $\delta\tilde{\boldsymbol{u}}\left(\boldsymbol{x}_i\right) \equiv \delta\tilde{\boldsymbol{u}}_i$ of the node i, the unknown nodal force $\tilde{\boldsymbol{F}}_i^{\mathrm{B}}$ will perform some work that has to be equivalent to the work performed by the tractions acting on the two contiguous boundary elements. Thus, the following equivalence holds

$$\delta\boldsymbol{u}_i^{\intercal}\,\tilde{\boldsymbol{F}}_i^{\mathrm{B}} = \sum_{j=k}^{k+1}\int_{s_j}\delta\boldsymbol{u}^{\intercal}(\zeta)\,\boldsymbol{t}(\zeta)\,J(\zeta)\,d\zeta, \tag{60}$$

which, recalling the interpolation expressed in Eq.(52), may be written as

$$\delta\boldsymbol{u}_i^{\intercal}\,\tilde{\boldsymbol{F}}_i^{\mathrm{B}} = \sum_{j=k}^{k+1}\delta\tilde{\boldsymbol{u}}^{j\intercal}\left[\int_{s_j}\mathbf{N}(\zeta)^{\intercal}\,\mathbf{N}(\zeta)\,J(\zeta)\,d\zeta\right]\tilde{\boldsymbol{t}}^{j} = \sum_{j=k}^{k+1}\delta\tilde{\boldsymbol{u}}^{j\intercal}\mathbf{M}^{j}\tilde{\boldsymbol{t}}^{j}, \tag{61}$$

where the matrices $\mathbf{M}^j \in \mathbb{R}^{4\times4}$ stem from the integration over the considered elements of the shape functions matrices, while the vectors $\delta\tilde{\boldsymbol{u}}^j, \tilde{\boldsymbol{t}}^j \in \mathbb{R}^{4\times1}$ collect the components of displacements at the two end nodes belonging to the element j, so that

$$\delta\tilde{\boldsymbol{u}}^{k} = \begin{bmatrix}\delta\tilde{\boldsymbol{u}}_{i-1}\\ \delta\tilde{\boldsymbol{u}}_i\end{bmatrix} = \begin{bmatrix}\mathbf{0}\\ \delta\tilde{\boldsymbol{u}}_i\end{bmatrix}, \qquad \delta\tilde{\boldsymbol{u}}^{k+1} = \begin{bmatrix}\delta\tilde{\boldsymbol{u}}_i\\ \delta\tilde{\boldsymbol{u}}_{i+1}\end{bmatrix} = \begin{bmatrix}\delta\tilde{\boldsymbol{u}}_i\\ \mathbf{0}\end{bmatrix}. \tag{62}$$

Taking into account Eqs.(62), Eq.(61) may be rewritten

$$\delta\tilde{\boldsymbol{u}}_i^{\intercal}\,\tilde{\boldsymbol{F}}_i^{\mathrm{B}} = \delta\tilde{\boldsymbol{u}}_i^{\intercal}\sum_{j=k}^{k+1}\mathbf{M}_i^{j}\,\tilde{\boldsymbol{t}}^{j} \quad \Rightarrow \quad \tilde{\boldsymbol{F}}_i^{\mathrm{B}} = \sum_{j=k}^{k+1}\mathbf{M}_i^{j}\,\tilde{\boldsymbol{t}}^{j} \tag{63}$$

where $\mathbf{M}_i^j \in \mathbb{R}^{2\times4}$ is the sub-matrix extracted from $\mathbf{M}^j$ selecting the appropriate rows corresponding to the displacements associated with the node i. It is important to realise that Eq.(63) allows expressing $\tilde{\boldsymbol{F}}_i^{\mathrm{B}}$ in terms of the traction components associated with the two elements containing the node i; for two-node linear boundary elements such expression could be written as

$$\tilde{\boldsymbol{F}}_i^{\mathrm{B}} = \sum_{k=i-1}^{i+1}\mathbf{M}_k\,\tilde{\boldsymbol{t}}_k \tag{64}$$

where $\tilde{\boldsymbol{t}}_k$ collects the components of tractions associated with the node k and $\mathbf{M}_i \in \mathbb{R}^{2\times2}$. Once Eq.(64) is written for all the boundary element nodes belonging to Γ^B, the nodal forces $\mathbf{F}^{\mathrm{B}}$ appearing in Eq.(59) can be expressed in terms of the boundary tractions $\mathbf{T}^{\mathrm{B}}$ appearing in Eq.(55) as

$$\mathbf{F}^{\mathrm{B}} = \mathbf{M}\,\mathbf{T}^{\mathrm{B}}, \tag{65}$$

where $\mathbf{F}^{\mathrm{B}}, \mathbf{T}^{\mathrm{B}} \in \mathbb{R}^{2m\times 1}$ and $\mathbf{M} \in \mathbb{R}^{2m\times 2m}$, with m expressing the total number of boundary nodes/elements. Exploiting Eq.(65), Eq.(55) can be written in a form to be used in conjunction with the VE equations. In particular, remembering that $\mathbf{T}^{\mathrm{B}} = \mathbf{G}^{-1}\,\mathbf{H}\,\mathbf{U}^{\mathrm{B}}$, it is possible to write

$$\mathbf{F}^{\mathrm{B}} = \mathbf{M}\mathbf{T}^{\mathrm{B}} = \left(\mathbf{M}\mathbf{G}^{-1}\,\mathbf{H}\right)\,\mathbf{U}^{\mathrm{B}} = \mathbf{K}^{\mathrm{B}}\,\mathbf{U}^{\mathrm{B}}. \tag{66}$$

The above BEM equations can now be combined with the VEM equations, which can be rearranged as

$$\begin{bmatrix} \mathbf{K}_{\Gamma\Gamma} & \mathbf{K}_{\Gamma\Omega} \\ \mathbf{K}_{\Omega\Gamma} & \mathbf{K}_{\Omega\Omega} \end{bmatrix}^{\mathrm{V}} \begin{bmatrix} \mathbf{U}_{\Gamma} \\ \mathbf{U}_{\Omega} \end{bmatrix}^{\mathrm{V}} = \begin{bmatrix} \mathbf{F}_{\Gamma} \\ \mathbf{F}_{\Omega} \end{bmatrix}^{\mathrm{V}}, \tag{67}$$

with the interface conditions in Eq.(59) and with suitable external boundary conditions to obtain the problem solution.

4. Numerical tests

In this Section, the formulation developed above is assessed and four different applications are considered. In the first case study, the accuracy and robustness of the methodology is assessed by solving the elastic problem of a unit cell with some inclusions of involved shape. Then, after assessing the reliability of the developed method in reconstructing the local elastic fields, its application to the computational homogenization of fibre-reinforced composite materials is investigated in the second set of tests. In the third application, a three-point bending test involving a quasi-brittle concrete notched beam has been considered, to assess the accuracy of the implemented non-linear VE formulation for isotropic damage against cases available in the literature. The last application considers a unit cell consisting of a circular elastic fibre in epoxy matrix where partial debonding between fibre and matrix triggers damage onset and evolution.

All the numerical experiments have been performed using a computational code developed in house and written in `MATLAB`; the developed software addresses all the stages of the computations, starting from morphology generation and meshing, handles FEM, VEM and BEM elements in the processing stage as well as all the interface and post-processing subroutines.

4.1. Elastic analysis of a microstructure with multiple inclusions

In order to asses the accuracy and robustness of the proposed methodology, a test microstructure is analysed, under the plane strain assumption. The geometry of the microstructure, shown in

Fig.(4), is a two-dimensional square box with four inclusions of involved shape. The external edges of the square box are aligned with the global Cartesian reference system $x - y$.

The purpose of this numerical test is to compare the displacement and stress fields obtained with the developed technique with a benchmark finite element solution, obtained employing an unstructured mesh of linear triangular elements. The analysis of the microstructure is performed with three different set of homogeneous displacement boundary conditions corresponding to prescribed macro-strains $\bar{\epsilon}_{ij}$: two uniaxial macro-strains acting along the x and y directions (BC_x, BC_y) and a pure shear macro-strain acting to modify the angle between the axes $x - y$ (BC_{xy}). The values of the displacement components, enforced over all the nodes belonging to the external boundary Γ of the computational domain, is given by

$$u_i = \bar{\epsilon}_{ij}\, x_j \quad \forall \boldsymbol{x} \in \Gamma. \tag{68}$$

Additionally, a parametric analysis is also performed by varying the contrast of material properties between matrix and inclusions. Both phases are assumed to be linear elastic and isotropic in the plane of the analysis and their relevant mechanical properties are given in Table 1 in terms of Poisson's ratio ν and of the ratio $\frac{E_f}{E_m}$, between the Young's modulus of the inclusions E_f and the matrix E_m.

Table 1: Mechanical properties for the matrix and the inclusions.

Material Code	E_f/E_m	ν
M10	10	0.3
M100	100	0.3
M1000	1000	0.3

4.1.1. Benchmark finite element solutions

Before assessing the convergence of the proposed hybrid VE-BE scheme, some benchmark finite element solutions are selected by performing a h-convergence analysis on triangular meshes. The elastic problem is solved for each set of boundary conditions and for each material. When passing from a coarser to a finer mesh with a smaller average element size, and then a higher number of associated degrees of freedom N_{dof}, the *distance* between the two related FE solutions is assessed

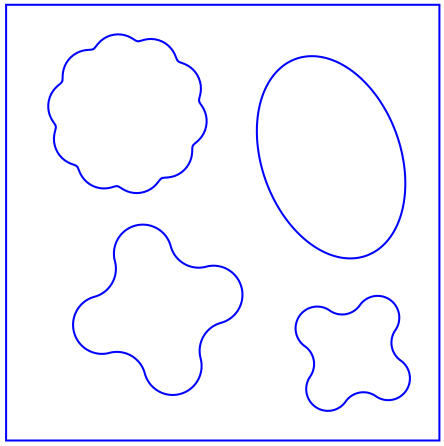

Fig. 4. Morphology of the considered unit cell.

employing a relative error measure for the displacement field e_u defined as

$$e_u = \left[\frac{\sum_{p=1}^{N_p} ||\boldsymbol{u}_a(\boldsymbol{x}_p) - \boldsymbol{u}_b(\boldsymbol{x}_p)||^2}{\sum_{p=1}^{N_p} ||\boldsymbol{u}_b(\boldsymbol{x}_p)||^2} \right]^{\frac{1}{2}} , \tag{69}$$

computed with reference to a fixed set of N_p sampling points p. In Eq.(69), $\boldsymbol{u}_a(\boldsymbol{x}_p)$ and $\boldsymbol{u}_b(\boldsymbol{x}_p)$ are the point-wise interpolated displacement vectors, computed at points having coordinates $\boldsymbol{x}_p$, for two different meshes a and b, where $h_a > h_b$ and $N_{dof,a} < N_{dof,b}$. Fig.(5) shows an example of triangular FE mesh and highlights the N_p fixed grid points selected for the computation of the measure given in Eq.(69). It is important to realise that such evaluation points are selected so to suitably sample the considered morphology and that they remain fixed as different meshes are considered; they will also be used to assess the accuracy of the hybrid virtual element - boundary element scheme with respect to the benchmark solution. An analogous relative error measure can be introduced for the stress field as

$$e_\sigma = \left[\frac{\sum_{p=1}^{N_p} ||\boldsymbol{\sigma}_a(\boldsymbol{x}_p) - \boldsymbol{\sigma}_b(\boldsymbol{x}_p)||^2}{\sum_{p=1}^{N_p} ||\boldsymbol{\sigma}_b(\boldsymbol{x}_p)||^2} \right]^{\frac{1}{2}} , \tag{70}$$

Table 2 reports information about the size and corresponding number of degrees of freedom for the considered FE meshes.

Table 3 reports the convergence data obtained by using the considered FE meshes. The generic column e_{ufi} reports, for the boundary condition and materials combination identified by the con-

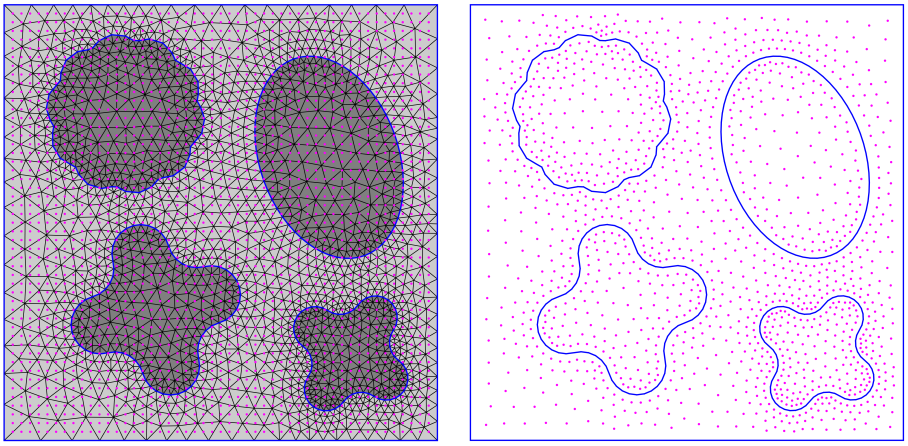

(a) (b)

Fig. 5. a) Example of a FE triangular mesh for the considered unit cell; b) Sampling points selected for the convergence analysis; their position remains fixed as the FE mesh is refined and the same sampling points will be employed to assess the performance of the VE-BE scheme.

Table 2: Features of the finite element meshes considered in the convergence analysis.

	F_1	F_2	F_3	F_4	F_5	F_6	F_7	F_8
N_{dof}	3574	10712	23612	36520	93104	144034	256142	575836
N_{el}	3483	10442	23210	36018	92302	143032	254804	573834

sidered rows, the relative error defined in Eq.(69) obtained by considering the coarser mesh F_i and the finer mesh F_{i+1}. Such results are graphically shown in Fig.(6). It is possible to note that, for all the considered Young's modulus ratios and for all the sets of boundary conditions, convergence may be considered achieved with the mesh F_5. The results obtained for this mesh are taken as benchmark for any further comparison.

The artificial linear sample shown in Fig.(4) has also been analysed by employing a pure boundary element approach for both the matrix and the inclusions. The adopted boundary element mesh is built starting from the nodes lying over the external boundary and the matrix/inclusion interfaces in the benchmark finite element mesh and consists of discontinuous linear elements for a total of 2788 nodes. The relative displacement error e_{ub} with respect to the benchmark FEM solutions (mesh F_5) for the three set of boundary conditions and for each material considered is reported in

Table 3: Convergence analysis for the considered FE solutions: $e_{uf\,i}$ represents the relative error between the displacement field computed with the mesh $i+1$ (finer) and that computed with the mesh i (coarser) at the selected sampling points.

		e_{uf1}	e_{uf2}	e_{uf3}	e_{uf4}	e_{uf5}	e_{uf6}	e_{uf7}
	M10	9.94e−4	4.01e−4	1.63e−4	8.75e−5	4.03e−5	3.27e−5	2.17e−5
BC_x	M100	1.34e−3	5.67e−4	2.24e−4	2.06e−4	5.58e−5	4.63e−5	3.10e−5
	M1000	1.38e−3	5.89e−4	2.32e−4	2.13e−4	5.79e−5	4.80e−5	3.21e−5
	M10	1.15e−3	4.82e−4	1.82e−4	1.64e−4	4.77e−5	3.96e−5	2.63e−5
BC_y	M100	1.61e−3	7.17e−4	2.61e−4	2.44e−4	6.99e−5	5.74e−5	3.84e−5
	M1000	1.68e−3	7.47e−4	2.71e−4	2.53e−4	7.29e−5	5.95e−5	3.97e−5
	M10	6.95e−4	3.07e−4	1.24e−4	1.07e−4	2.94e−5	2.45e−5	1.83e−5
BC_{xy}	M100	9.05e−4	4.32e−4	1.72e−4	1.50e−4	4.03e−5	3.40e−5	2.55e−5
	M1000	9.32e−4	4.46e−4	1.79e−4	1.54e−4	4.17e−5	3.51e−5	2.63e−5

Table 4.

Table 4: Relative displacement error e_{ub} of the BE solutions with respect to the benchmark FEM solutions.

	BC_x	BC_y	BC_{xy}
M10	9.30e−5	1.23e−4	7.12e−5
M100	1.34e−4	1.81e−4	1.02e−4
M1000	1.39e−4	1.87e−4	1.05e−4

4.1.2. Virtual element solutions

In this Section, the morphology shown in Fig.(4) is analysed by employing a pure virtual element approach. Fig.(7a) shows an example polygonal mesh of the considered morphology, built by using the meshing strategy described in Section 2. Table 5 summarises the features of the five polygonal mesh refinements used to assess the convergence of the virtual element scheme with respect to the benchmark finite element solution. In particular e_{uvi} represents the relative error for displacements, with respect to the reference FE solution, of the virtual element solution obtained by the *i-th* virtual element mesh V_i, computed using Eq.(69). Analogously, Table 7 reports a global measure of relative error for the stress vector computed by the virtual element method, with respect to the stresses

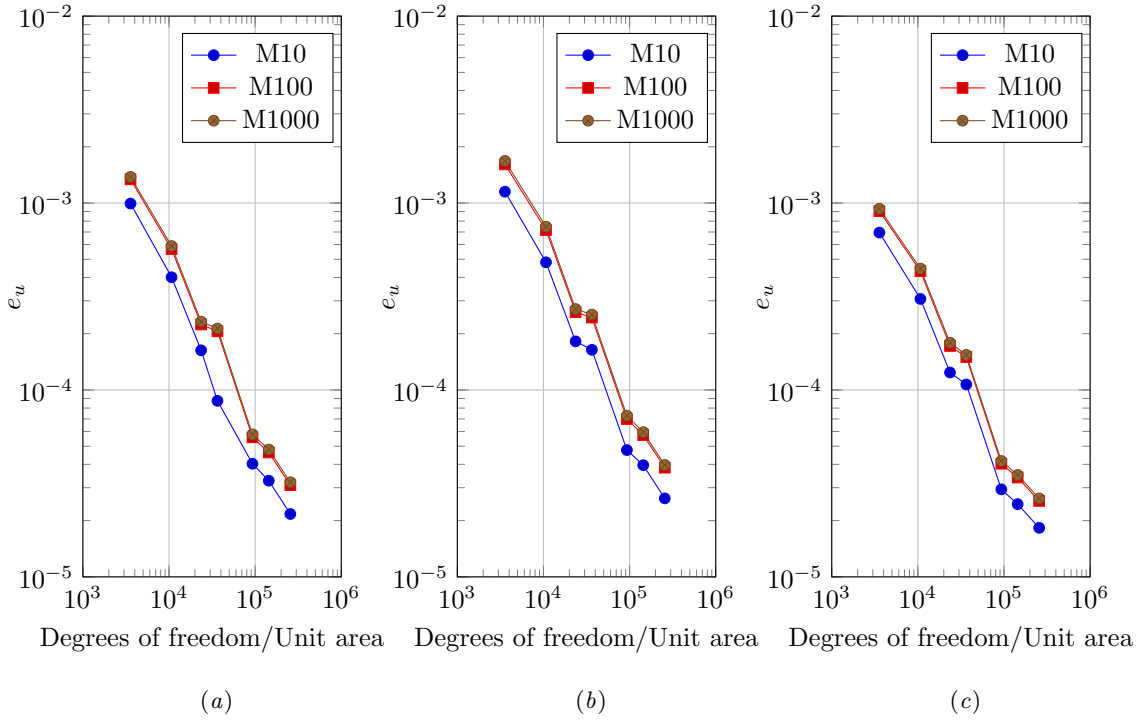

Fig. 6. Convergence of the FE solutions: displacements relative error e_u for (a) BC_x, (b) BC_y, (c) BC_{xy}.

provided by the reference FE solution.

Table 5: Features of the polygonal mesh refinements used for the virtual element analysis of the considered morphology.

	V_1	V_2	V_3	V_4	V_5
N_{dof}	16516	30616	60388	98140	132844
N_{el}	4128	7653	15096	24534	33210

575 *4.1.3. Hybrid virtual-boundary element solutions*

In this section, the developed hybrid virtual-boundary element scheme is employed to analyse the reference morphology in Fig.(4). Fig.(7b) shows an example discretisation of the considered morphology employed for the hybrid analysis, built by using the strategy described in Section 2. Table 8 reports some features of the mesh employed for the hybrid analysis, highlighting the number

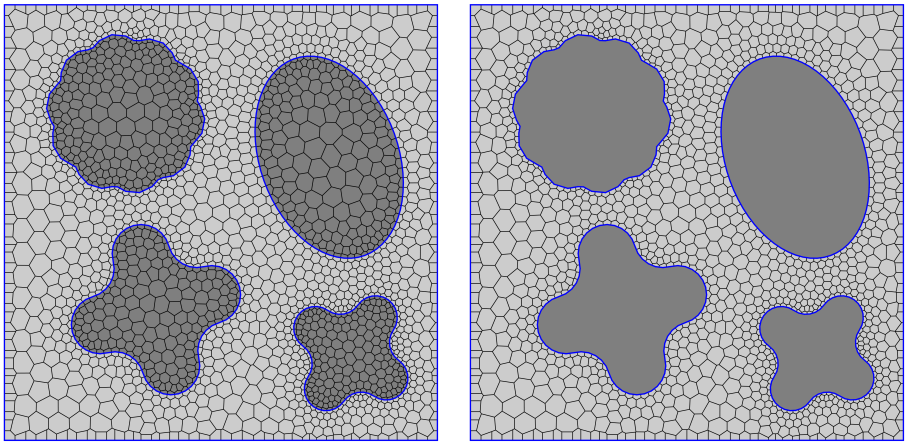

(a) (b)

Fig. 7. a) Example polygonal mesh for the virtual element analysis; b) Example mesh for the hybrid virtual element - boundary element analysis.

Table 6: Relative displacement error e_u with respect to the benchmark FEM solutions of the VE solutions obtained by using the considered progressive polygonal mesh refinements.

		e_{uv1}	e_{uv2}	e_{uv3}	e_{uv4}	e_{uv5}
	M10	6.30e−4	3.70e−4	1.63e−4	8.58e−5	6.57e−5
BC_x	M100	9.19e−4	5.41e−4	2.37e−4	1.28e−4	9.45e−5
	M1000	9.58e−4	5.63e−4	2.48e−4	1.35e−4	9.98e−5
	M10	8.89e−4	4.92e−4	2.06e−4	1.11e−4	8.21e−5
BC_y	M100	1.37e−3	7.55e−4	3.21e−4	1.78e−4	1.25e−4
	M1000	1.43e−3	7.91e−4	3.39e−4	1.90e−4	1.34e−4
	M10	5.14e−4	2.67e−4	1.22e−4	6.43e−5	4.50e−5
BC_{xy}	M100	7.02e−4	3.72e−4	1.76e−4	9.17e−5	6.33e−5
	M1000	7.46e−4	3.86e−4	1.85e−4	9.60e−5	6.65e−5

of both 2D polygonal virtual elements and 1D linear continuous boundary elements employed in the analyses. Table 9 show the error, computed using Eq.(69), of the displacements field reconstructed using the hybrid strategy with respect to the FE benchmark solution, while Table 10 reports data about the measure of the relative error in the stress field computed using Eq.(70).

Table 7: Relative stress error e_σ with respect to the benchmark FEM solutions of the VE solutions obtained by using the considered progressive polygonal mesh refinements.

		$e_{\sigma v1}$	$e_{\sigma v2}$	$e_{\sigma v3}$	$e_{\sigma v4}$	$e_{\sigma v5}$
	M10	2.74e−2	2.65e−2	2.09e−2	1.98e−2	1.94e−2
BC_x	M100	4.15e−2	4.13e−2	3.18e−2	3.16e−2	3.05e−2
	M1000	4.40e−2	4.41e−2	3.38e−2	3.39e−2	3.27e−2
	M10	2.96e−2	2.98e−2	2.34e−2	2.30e−2	2.19e−2
BC_y	M100	4.61e−2	4.82e−2	3.69e−2	3.79e−2	3.61e−2
	M1000	4.90e−2	5.16e−2	3.93e−2	4.07e−2	3.88e−2
	M10	6.71e−2	5.89e−2	5.12e−2	4.21e−2	3.92e−2
BC_{xy}	M100	9.28e−2	7.77e−2	7.29e−2	5.69e−2	5.41e−2
	M1000	9.68e−2	8.05e−2	7.64e−2	5.92e−2	5.63e−2

Table 8: Features of the hybrid virtual-boundary element mesh refinements employed in the comparative analysis. The total number of degrees of freedom N_{dof}, the number of virtual elements $N_{\mathrm{VE}s}$ and the number of boundary elements $N_{\mathrm{BE}s}$ are reported.

	H_1	H_2	H_3	H_4	H_5	H_6
N_{dof}	11060	20496	39960	64656	87424	124248
$N_{\mathrm{VE}s}$	2614	4903	9703	15841	21459	30561
$N_{\mathrm{BE}s}$	584	864	1128	1272	1568	1984

Figs.(8-9) compare graphically the convergence of the hybrid virtual-boundary element solution with that of the pure virtual element solution. For both techniques the accuracy of the solution is measured with respect to the assumed benchmark solution, for all the investigated combinations of boundary conditions and materials. Specifically, the plots report the relative error measures of displacement and stress versus the number of degrees of freedom per unit area employed in the analysis. It is observed that, in this sense, the convergence of the hybrid solution is quicker with respect to the convergence of the pure virtual element scheme, both for the displacement and the stress fields. However, while for the displacement field the two techniques show closer convergence rates, it emerges that, for the stress field, the hybrid VE-BE technique approaches convergence noticeably more rapidly that the pure virtual element scheme, at least when measured with respect

Table 9: Relative displacement error e_u with respect to the benchmark FEM solutions of the hybrid VE-BE solutions obtained by using the considered progressive mesh refinements.

		e_{uh1}	e_{uh2}	e_{uh3}	e_{uh4}	e_{uh5}	e_{uh6}
	M10	5.93e−4	3.33e−4	1.51e−4	8.39e−5	6.97e−5	6.35e−5
BC_x	M100	8.99e−4	5.23e−4	2.31e−4	1.23e−4	9.19e−5	7.29e−5
	M1000	9.55e−4	5.61e−4	2.47e−4	1.34e−4	9.92e−5	7.50e−5
	M10	8.08e−4	4.29e−4	1.91e−4	1.09e−4	9.01e−5	8.43e−5
BC_y	M100	1.32e−3	7.21e−4	3.09e−4	1.69e−4	1.21e−4	9.79e−5
	M1000	1.43e−3	7.86e−4	3.37e−4	1.88e−4	1.33e−4	1.01e−4
	M10	4.61e−4	2.40e−4	1.08e−4	6.13e−5	4.99e−5	4.76e−5
BC_{xy}	M100	6.97e−4	3.61e−4	1.69e−4	8.73e−5	6.20e−5	5.38e−5
	M1000	7.44e−4	3.85e−4	1.84e−4	9.55e−5	6.63e−5	5.52e−5

Table 10: Relative stress error e_σ with respect to the benchmark FEM solutions of the hybrid VE-BE solutions obtained by using the considered progressive mesh refinements.

		$e_{\sigma h1}$	$e_{\sigma h2}$	$e_{\sigma h3}$	$e_{\sigma h4}$	$e_{\sigma h5}$	$e_{\sigma h6}$
	M10	2.06e−2	1.87e−2	1.69e−2	1.58e−2	1.59e−2	1.54e−2
BC_x	M100	2.92e−2	2.69e−2	2.47e−2	2.36e−2	2.37e−2	2.33e−2
	M1000	3.09e−2	2.85e−2	2.62e−2	2.52e−2	2.52e−2	2.48e−2
	M10	2.29e−2	2.09e−2	1.89e−2	1.78e−2	1.73e−2	1.76e−2
BC_y	M100	3.37e−2	3.13e−2	2.88e−2	2.77e−2	2.73e−2	2.74e−2
	M1000	3.58e−2	3.33e−2	3.07e−2	2.96e−2	2.92e−2	2.93e−2
	M10	4.59e−2	4.15e−2	3.47e−2	3.33e−2	3.20e−2	3.21e−2
BC_{xy}	M100	5.68e−2	5.19e−2	4.57e−2	4.42e−2	4.31e−2	4.32e−2
	M1000	5.86e−2	5.36e−2	4.75e−2	4.60e−2	4.49e−2	4.50e−2

to the number of DOFs per unit area. The reason of such behaviour is twofold: *i*) in the hybrid technique, the nodes within the inclusions are removed, due to the employment of the boundary integral formulation, which contributes to the reduction in the number of DOFs per unit area, this explaining the convergence patterns observed for the displacement field; *i*) in the hybrid scheme, the stresses within the inclusion are computed by employing, in post-processing, the boundary

integral representation given in Eq.(57), which generally ensures higher accuracy, with respect to standard FE methods, in the reconstruction of the internal stresses. The interplay between the reduction in the number of DOFs associated to nodes within the inclusions and better rendering of the stresses due to the employment of the boundary integral representation of stresses explains the convergence patterns shown in Fig.(9). Eventually Fig.(10) shows the plot of stress components σ_{xx}, σ_{yy} and σ_{xy}, corresponding to an enforced uniaxial strain $\bar{\epsilon}_{xx} = 0.05$, computed with the finite element benchmark scheme, the virtual element implementation and the hybrid strategy, highlighting satisfying agreement among the three schemes.

4.2. Computational homogenization of fibre-reinforced composites

This section describes the application of the proposed method to the computational homogenization of unidirectional fibre-reinforced composites. In computational homogenization, the macroscopic material properties are computed by simulating the micro-scale response of properly selected material domains, referred to as *unit cells*, and then averaging, over such domains, the fields of interest, with the aim of identifying macroscopic links between such averaged quantities. Unit cells become *representative volume elements* (RVEs) when they can be considered representative of the mechanical behaviour of the material at the macro-scale. Interested readers are referred to Ref.[65] for an in-depth treatment of materials homogenization.

This test case is presented in this study for the following reason. One of the strategies employed for the computational homogenization of heterogeneous materials is based on the generation of a certain number of artificial digital samples of the considered material, with random features, and on the computation of the ensemble averages, over the set of considered specimens, of suitably volume averaged quantities, either stresses of strains, see e.g. Refs.[66, 67, 20]. In this procedure, it is important to ensure a suitable mesh quality for all the generated random microstructures, which may result in a particularly challenging task. It is believed that the inherent features of VEM may benefit the meshing procedures in this kind of problems, i.e. when a certain number of morphologies with statistical features need to be considered.

The unit cells for the present test lie in the plane $x_2 - x_3$, normal to the axes of the fibres, which are parallel to the axis x_1. They are generated by randomly scattering a given number of arbitrarily shaped inclusions in a rectangular domain, through an algorithm avoiding pathological superposition of the inclusions. The inclusions considered here present the transversal section shown

in Fig.(11), are all of the same size and have and random orientation θ with respect to the x_2 axis. The average number of inclusions is determined by the parameter $\delta = L/r$, where L is the unit cell's side length and r is the radius of the circle that circumscribes the fibre inclusion. Fig.(12) shows two example geometries for a random microstructure and the subsequent VE-BE discretisations for $\delta = 20$ and $\delta = 45$.

The material constants of the composite constituents, isotropic in the $x_2 - x_3$ plane, are given in Table 11, in terms of transverse Young modulus E_{22} and transverse shear modulus G_{23}. Assuming a Poisson random distribution of fibres within the unit cell, and considering the in-plane isotropy of the constituents, the composite will be isotropic in the plane $(x_2 - x_3)$ at the macroscopic level. Its transverse behaviour is then completely defined by two elastic modula. In this study the plain strain bulk modulus $\bar{K}_{23}$ and the transverse shear modulus $\bar{G}_{23}$ are considered.

Table 11: Material properties for epoxy matrix and carbon fibres in transverse direction, as taken from Ref.[68].

Mechanical Properties	E_{22} [GPa]	G_{23} [GPa]
AS4 carbon fibres	15	7
3501-6 epoxy matrix	4.2	1.567

The problem of determining the appropriate size of the unit cell, or the appropriate number of inclusions within it, so to identify a RVE has been extensively investigated in the literature [69, 66, 70, 71, 72, 73, 74]. In general, given a random microstructural sample subjected to a suitable set of boundary conditions, see e.g. [66], the link between homogenised stresses and strains is provided by *apparent* properties, which may not be representative of the macro-material if the microstructural sample, or unit cell, is too small. As the unit cell size or the number of inclusions within it increase, the unit cell becomes more representative of the macro-material and the apparent properties approach the *effective* properties. Besides considering the behaviour of the averaged properties versus the size or number of inclusions of the unit cell, the homogenization procedure can be enriched by considering *ensemble* averages of the volume homogenized properties over a set of unit cells with the same size and number of inclusions, but different spatial distribution of the inclusions themselves. The procedure generally produces an estimate of the effective properties with unit cells smaller with respect to the case in which only individual microstructures are considered, see e.g. Ref.[66] for a detailed discussion. In the present study this homogenization procedure is

used. The interested readers are referred to Refs.[67, 20] for further examples about the application of the methodology .

For the considered composite, sets of unit cells at varying values of the parameter δ are considered, while the fibre volume fraction is kept constant at $V_f = 0.25$. For each value of δ, $N_s = 50$ different random sample micro-morphologies have been generated and analysed using the proposed hybrid approach. Each unit cell $\mathcal{U}_m$, comprising a number of randomly located and orientated inclusions as in Fig.(12), has been discretised using arbitrary polygonal virtual elements for the matrix and a single boundary element domain for each inclusion. Each $\mathcal{U}_m$ is the subjected to three linearly independent sets of displacement boundary conditions, corresponding to three sets of enforced macro-strains expressed in Voigt notation as $\bar{\boldsymbol{\epsilon}} = \{\bar{\epsilon}_{22}, \bar{\epsilon}_{33}, 2 \cdot \bar{\epsilon}_{23}\}$. More specifically, the unit cells are loaded through displacements given by Eq.(68), where the following three sets of macro-strains

$$\bar{\boldsymbol{\epsilon}}^{\,a} = \{1, 0, 0\}\,, \qquad \bar{\boldsymbol{\epsilon}}^{\,b} = \{0, 1, 0\}\,, \qquad \bar{\boldsymbol{\epsilon}}^{\,c} = \{0, 0, 1\} \tag{71}$$

are considered. Once a prescribed boundary condition is enforced, the microstructural problem is solved employing the proposed hybrid scheme, thus providing the micro-displacement, strain and stress fields within the microstructure. The averaged stresses $\bar{\boldsymbol{\sigma}} = \{\bar{\sigma}_{22}, \bar{\sigma}_{33}, \bar{\sigma}_{23}\}$ are then computed as volume averages of the local micro-stress tensor over the domain of the unit cells, as

$$\bar{\sigma}_{ij} = \frac{1}{\Omega} \int_{\Omega} \sigma_{ij}\left(\boldsymbol{x}\right) d\Omega = \frac{1}{\Omega} \left(\int_{\Omega^V} \sigma_{ij}\left(\boldsymbol{x}\right) d\Omega + \int_{\Omega^B} \sigma_{ij}\left(\boldsymbol{x}\right) d\Omega \right), \tag{72}$$

where the domain integral is subdivided into contributions coming separately from the VE and BE regions. The integral over the BE regions can be further expressed as a sum of integrals over each BE modelled inclusion Ω_k^B, and it may be demonstrated that

$$\int_{\Omega^B} \sigma_{ij}\left(\boldsymbol{x}\right) d\Omega = \sum_i \int_{\Omega_k^B} \sigma_{ij}\left(\boldsymbol{x}\right) d\Omega = \sum_i \int_{\Gamma_k} t_i \, n_j \, d\Gamma, \tag{73}$$

which implies that the integration of stresses over the BE inclusions only require the computation of integrals along the boundary Γ_k^B of the inclusion of the traction components t_i, which are readily available from the BE solution, thus avoiding the more expensive use of Eq.(57). The use of Eq.(73) into Eq.(72) allows remarkable computational savings in computational homogenization problems and constitutes a benefit of the presented technique.

For a given unit cell $\mathcal{U}_m$, the computation of the averaged stresses corresponding to the three considered sets of boundary conditions given in Eq.(71) allows populating the columns of the ap-

parent elastic matrix $\bar{\mathbf{C}}_m$, which links averaged stresses and strains according to

$$\bar{\boldsymbol{\sigma}} = \bar{\mathbf{C}}_m \, \bar{\boldsymbol{\epsilon}}. \tag{74}$$

For each value of the parameter δ, once the components of $\bar{\mathbf{C}}_m$ are computed for all the $N_s = 50$ generated random unit cells, a macroscopic *apparent* constitutive matrix $\langle \bar{\mathbf{C}} \rangle$ is computed from the ensemble average of the components of $\bar{\mathbf{C}}_m$ over the N_s samples, i.e.

$$\langle \bar{\mathbf{C}} \rangle = \frac{1}{N_s} \sum_{m=1}^{N_s} \bar{\mathbf{C}}_m. \tag{75}$$

The apparent transverse elastic properties $\bar{K}_{23}$ and $\bar{G}_{23}$ associated to the considered value of δ are eventually obtained from the ensemble averaged matrix $\langle \bar{\mathbf{C}} \rangle$.

Fig.(13) shows the values of $\bar{K}_{23}$ and $\bar{G}_{23}$ versus δ in plain strains, reporting both the values corresponding to individual samples $\mathcal{U}_m$ and the ensemble averaged values. In general, the scatter of the individual values decreases as δ increases, as the unit cells approach the RVE by including a higher number of fibres. In the literature, several theoretical models have been introduced to provide rigorous bounds for the effective macroscopic properties of heterogeneous materials. In the present study, the computed effective material properties are compared with the Hashin-Hill bounds [75, 76], identified in Fig.(13) by the boundaries of the grey region: it is observed that the values computed through the developed technique fall within such bounds, confirming its usefulness in computational homogenization applications.

4.3. Three-point bending test with damage

In this section, the implemented VEM for isotropic damage modelling is validated. A the three-point bending (TPB) test is considered as benchmark: it investigates damage initiation and evolution up to failure of a notched concrete beam, where the damage growth is dominated by mode I loading.

Geometry and boundary conditions for this problem are shown in Fig.(14). The beam has square cross-section of side $H = 100\,\text{mm}$ and spans $W = 450\,\text{mm}$. The notch is $A = 5\,\text{mm}$ wide and extends up to one half of the beam height. These dimensions correspond to the experiments performed in Ref.[77]. The material's Young's modulus is $E = 20\,000\,\text{MPa}$ and the Poisson's ratio is $\nu = 0.2$. The law with exponential softening defined in Eq.(44) is adopted to model damage evolution. The damage parameters are chosen as in Ref.[51] as $\varepsilon_0 = 9.0\text{e}{-5}$ and $\varepsilon_f = 7.0\text{e}{-3}$. The equivalent

strains τ are computed following the definition of Mazars in Eq.(40) and the nonlocal interaction radius is set to $R = 4\,\text{mm}$. The tests have been performed, under plane strain assumptions, using three different meshes of polygonal elements to determine convergence with mesh refinement. The two coarser meshes, referred to as V1 and V2, contains 6072 and 8493 elements and are shown in Fig.15. A further finer mesh, referred to as V3, is considered an over-kill discretisation and it contains 18546 polygonal elements .

The simulations are performed in displacement control using a Newton-Raphson scheme. Results are observed in terms of force versus displacement at the point where the vertical displacement is applied and compared with experimental results from Ref.[77] and with numerical results from Ref.[51]. The computed force-displacement curves, the reference numerical solution from Ref.[51] and the experimental bounds from Ref.[77] are depicted in Fig.(16). For all the considered discretisations, they reveal good agreement with the experimental bounds for the most part of the force-displacement diagram. Comparison with the reference numerical solution obtained with full integrated 4-node bilinear isoparametric elements and mesh size of 1.67 mm, shows a better reproduction of the experimental data in the first part of the softening branch. A slight underestimation of the computed load can be noticed in the last part of the curve's softening branch. This difference, already noted in Ref.[11], where a similar numerical test with polygonal virtual elements has been performed, is likely due to the unstructured character of the virtual element mesh with respect to the finite element reference mesh. The evolution of the damage profile is shown in Fig.(17): damage originates at the bottom of the notch and grows in a limited zone along the structure vertical axis of symmetry.

The presented results validate the implemented VE isotropic damage model, which will be used in the next computational test.

4.4. Transverse failure of a composite fibre-reinforced unit cell

In the present Section, the hybrid virtual-boundary element formulation, combined with an isotropic damage model for the regions modelled with virtual elements, is used in the computational simulation of the damage evolution under transverse tensile loading of a unit cell comprising a single fibre embedded in an epoxy matrix, with initial partial debonding between fibre and matrix. The study of such fibre-matrix system has been the subject of a considerable number of studies [78, 79, 80, 81, 82, 83].

The test case is shown in Fig.(18). In the initial configuration, it is assumed that the circular fibre is debonded from the matrix in the interface region identified by $|\theta_d| =\leq 70°$, see Ref.[80]. Outside the debonded region, the inclusion is perfectly bonded to the matrix. This test aims to simulate the progression into the matrix of the two kinked cracks that start from both ends of the debonded zone and this initial condition is assumed as no cohesive interfaces have been included so far in the model, which identifies a direction of further development.

The fibre diameter is $D = 0.025\,\text{mm}$, and the side length of the unit cell is $L = 0.2\,\text{mm}$, giving a corresponding volume fraction $V_f = 0.0123$. The center of the circle coincides with the center of the square. The tensile loading is applied by prescribing uniform displacements $\bar{u}$ at the sample left and right edges. Plane strain conditions are assumed. The fibre material is assumed linear elastic and it does not develop damage. The matrix materials is treated as linear elastic until the damage onset, which is governed by the loading function in Eq.(41). The exponential damage evolution law in Eq.(44) is assumed, with $r_0 = 1$, $r_f = 234$, according to strength and fracture toughness data about epoxy, and $R = D/3$. The transverse elastic material parameters are $E_F = 201\,\text{GPa}$ and $\nu_F = 0.22$ for the fibre and $E_M = 2.8\,\text{GPa}$ and $\nu_M = 0.33$ for the matrix. The fracture toughness of the epoxy matrix is $G_{fr} = 0.09\,\text{N/mm}$.

To make the mesh consistent with the parameter assumed in the non-local continuum damage model, the matrix region is discretised with 8047 2D lowest-order virtual polygon elements, which induce 256 1D linear boundary elements on the fibre-matrix interface, where conformal meshes are employed. The overall mesh is shown in Fig.(19). The simulations are performed under displacement control using a Newton-Raphson with adaptive load step, to track the steep softening branch. The simulation is arrested at a nominal macro-strain $\varepsilon_x = 0.05$. For each load increment, the plotted reaction force is computed as the sum of the nodal reaction forces on the right edge.

Fig.(20) shows the load-displacement diagram; the identified labes correspond to the damage profiles shown in Fig.(21). Linear elastic behaviour is exhibited up to slightly before the point (a) in the curve, which marks the initiation of damage at the ends of the debonded interface, where stress concentration is expected. Once damage is activated, the two symmetric damaged/failed region progress within the matrix, following a kinked path consistent with the behaviour reported in Refs.[84, 80]. As the loading increases, the material failure evolves affecting regions oriented perpendicularly with respect to the load direction, up to the unit cell boundary, which causes a progressive decrease of the load-carrying capability identified by the softening branch of the load-

displacement diagram.

5. Discussion

In this contribution a hybrid computational technique has been developed for the analysis of multi-region two-dimensional problems for applications in computational micro-mechanics and homogenization. The method suggests the simultaneous use of the recently emerged virtual element method and of the highly accurate boundary element method. Each of the two techniques offers some definite advantages.

The virtual element method can be seen as an effective generalisation of the finite element method to meshes including elements of very general shape, including general polygonal elements, non-convex elements, highly distorted elements and elements with curved edges. The use of VEM in addressing complex mesh morphologies and problems inducing high mesh distortion has been demonstrated in the literature, as discussed in the *Introduction*. In the present framework, mostly addressed at materials micro-mechanics, the advantages offered by VEM are twofold: *i*) in general, the method offers a powerful tool for meshing morphologically complex domains, as those often encountered in statistical homogenization procedures, see e.g. Fig.(12), in which the regularity of the regions related to the different phases cannot be *a-priori* assumed; *ii*) thanks to the possibility of extending to VEM the features of FEM, in particular its generality in dealing with non-linear constitutive behaviours, in the proposed framework the method can be employed for meshing phases likely to exhibit, in the loading process, non-linear behaviours such as plasticity, viscosity or damage [30]. This is the case of composite materials subjected to loading able to initiate visco-plastic flows and/or damage in the matrix.

On the other hand, the boundary element method has proven effective in the accurate reconstruction of the elastic fields through a discretization procedure involving only the boundary of the analysed domains, thanks to the underlying integral formulation, alternative to methods based on the weak formulation of the considered boundary value problems. In particular, BEM is known for being able to provide accurate solutions at reduced computational costs [19]. The method can be used for analysing non linear problems, although its employment in linear problems is more widespread and straightforward. In the proposed framework, the use of BEM is suggested for modelling microstructural phases not expected to develop non-linear constitutive behaviour. This use

is beneficial for two reasons, as already mentioned in the previous section: *i*) it allows to reduce the number of DOFs needed for modelling the inclusions, thus reducing the computational burden of the analysis; *ii*) it generally provides a more accurate representation of stresses within the inclusions, thus inducing a faster convergence in the stress fields, as shown in Figs.(8-9).

Several directions of further investigation may be identified for the proposed framework.

As mentioned in Section 3.1.3, in this contribution the lowest order VEM, $k = 1$, has been employed as it allows a straightforward coupling with the BE model of the inclusions. However, higher order virtual element formulations have been proposed in the literature [40, 39, 4]. Higher order formulations are based on: *i*) the definition of a local virtual element space, for trial and test functions, which contains the set of all polynomial functions up to the selected degree k *plus* a set of additional functions, whose explicit knowledge is never required for the construction of the method; *ii*) the selection of a suitable set of degrees of freedom, grouped into a set *boundary* degrees of freedom, associated to the element vertices and to points lying on their edges, which maintain the physical meaning of displacements, *plus* a set of *internal* degrees of freedom, which represents suitably defined integrals, or moments, over the elements, of the functions belonging to the local virtual element space. If the virtual element space and the degrees of freedom are properly chosen, the entries of the local stiffness matrix can be computed without the explicit knowledge of the unknown additional functions. As an example, a VEM of order $k = 2$ would imply a quadratic approximation of the displacements over the edges of the virtual elements, expressed in terms of nodal displacements associated to the vertices and to the mid points of the edges, which could be readily coupled with a quadratic formulation of the boundary element model of the inclusions. The coupling between higher order virtual elements and higher order boundary elements could be a direction of further research and could lead to remarkable benefits in terms of solution accuracy.

An important caveat about the use of BEM is related to the fact that the method induces non-symmetric and non-definite fully populated solving matrices, see e.g. Ref.[60]. As long as the number of elements used for modelling each inclusion is limited, this does not require additional consideration and the potential of BEM in reducing the computational burden is preserved. However, should an inclusion need several hundreds boundary elements, the presence of fully populated blocks in the solving systems could reduce the effectiveness of the computation and increase the computational costs. These aspects could be mitigated and effectively addressed by using fast iterative solvers in conjunction with special matrix representations, e.g. fast multipoles [85] or

hierarchical matrices [86, 87, 88, 89].

Another aspect to be addressed in the framework of BEM and its coupling with VEM, is the consideration of inclusions with sharp corners. The consideration of such geometrical entities is generally known to be problematic in BEM, due to the non unique definition of the normal at the corners. Some strategies to address such an issue have been proposed in the literature [19, 90], consisting in the employment of semi-discontinuous elements or hyper-singular traction boundary integral equations, and their inclusion in the present framework could be investigated in future studies.

Eventually, it is worth noting that the present technique has been hitherto developed only for two-dimensional problems. Although the considered test cases allow highlighting the potential benefits of the proposed method, 2D models generally present strong limitations in the computation of the effective properties of real materials, as they often neglect important inherent three-dimensional morphological or physical material features. In fact, while in this work the scheme has been successfully employed to compute the transverse elastic constants of composite laminae reinforced by unidirectional fibers, it would not be possible to employ it to compute the in-plane properties, or even the transverse properties, of laminates with general lay-ups, due to the impossibility of rendering in a 2D scheme the inherent 3D morphological features related to mutual orientation of the fibers belonging to different contiguous laminae. For such reasons, an interesting direction of further research could be related to the extension of the proposed scheme to three-dimensional problems. In the literature, three-dimensional formulations have been developed both for VEM and BEM, see e.g. Refs.[7, 19]. The coupling between the two techniques in the 3D case could be readily applied, for example, to the computational homogenisation of polycrystalline materials, which has been successfully addressed separately both with VEM [14] and BEM [20, 91, 23, 25], both in the case of linear and non-linear material behaviour. Polycrystals represent another class of materials for which three-dimensional effects, related to mutual orientation of the crystallographic lattices of different grains in the 3D space, play an important role in the determination of the macroscopic effective properties.

The extension of the framework to the analysis of multi-phase microstructures exhibiting general non-linear behaviours, along the lines discussed above, and to the analysis of three-dimensional micro-morphologies, as well as a comprehensive investigation about the computational advantages offered by the framework, will form the object of further investigations.

6. Conclusions

A hybrid computational method based on the conjoined use of the recently emerged virtual element method and the boundary element method has been formulated, developed and implemented for the analysis of two-dimensional multi-region problems for applications in computational micro-mechanics. The method has been applied to the elastic analysis and computational homogenization of fibre reinforced composite materials and, by implementing an isotropic damage VEM, for the analysis of matrix degradation in a composite unit cell under progressive loading. The analysed case studies show how the method offers accurate and reliable numerical results and how the inherent properties of the virtual element and boundary element methods can be exploited in the analysis of complex materials micro-morphologies. It is found that the hybrid technique, due to the features of the boundary integral formulation underlying the boundary element method, offers faster convergence with respect to a purely virtual element approach. The employment of the VEM, on the other hand, allows the straightforward inclusion of non-linear phenomena, such as material degradation, in the framework. The results appear promising and further research could be directed at the development of a framework addressing multiphase materials exhibiting both linear and general non-linear phases, for which the respective benefits of the boundary and virtual element approaches could be optimally tailored.

Acknowledgements

The authors acknowledge the support of the *Italian Ministry of Education, University and Research* – MIUR – through the project DEVISU, funded under the scheme PRIN-2107 – Grant 22017ZX9X4K_006.

[1] K. Alberi, M. B. Nardelli, A. Zakutayev, L. Mitas, S. Curtarolo, A. Jain, M. Fornari, N. Marzari, I. Takeuchi, M. L. Green, M. Kanatzidis, M. F. Toney, S. Butenko, B. Meredig, S. Lany, U. Kattner, A. Davydov, E. S. Toberer, V. Stevanovic, A. Walsh, N.-G. Park, A. Aspuru-Guzik, D. P. Tabor, J. Nelson, J. Murphy, A. Setlur, J. Gregoire, H. Li, R. Xiao, A. Ludwig, L. W. Martin, A. M. Rappe, S.-H. Wei, J. Perkins, The 2019 materials by design roadmap, Journal of Physics D: Applied Physics 52 (1) (2018) 013001. doi:10.1088/1361-6463/aad926.

[2] E. B. Tadmor, R. E. Miller, Modeling materials: continuum, atomistic and multiscale techniques, Cambridge University Press, 2011.

[3] L. Beirão da Veiga, F. Brezzi, A. Cangiani, G. Manzini, L. D. Marini, A. Russo, Basic principles of virtual element methods, Mathematical Models and Methods in Applied Sciences 23 (01) (2013) 199–214.

[4] L. Beirão da Veiga, F. Brezzi, L. D. Marini, A. Russo, The hitchhiker's guide to the virtual element method, Mathematical models and methods in applied sciences 24 (08) (2014) 1541–1573.

[5] L. B. Da Veiga, A. Russo, G. Vacca, The virtual element method with curved edges, ESAIM: Mathematical Modelling and Numerical Analysis 53 (2) (2019) 375–404.

[6] F. Brezzi, L. D. Marini, Virtual element methods for plate bending problems, Computer Methods in Applied Mechanics and Engineering 253 (2013) 455 – 462. doi:https://doi.org/10.1016/j.cma.2012.09.012.
URL http://www.sciencedirect.com/science/article/pii/S0045782512002940

[7] A. L. Gain, C. Talischi, G. H. Paulino, On the virtual element method for three-dimensional linear elasticity problems on arbitrary polyhedral meshes, Computer Methods in Applied Mechanics and Engineering 282 (2014) 132–160.

[8] P. Wriggers, W. Rust, B. Reddy, A virtual element method for contact, Computational Mechanics 58 (6) (2016) 1039–1050.

[9] X. Peng, E. Atroshchenko, P. Kerfriden, S. Bordas, Isogeometric boundary element methods for three dimensional static fracture and fatigue crack growth, Computer Methods in Applied Mechanics and Engineering 316 (2017) 151 – 185, special Issue on Isogeometric Analysis: Progress and Challenges. doi:https://doi.org/10.1016/j.cma.2016.05.038.
URL http://www.sciencedirect.com/science/article/pii/S0045782516304832

[10] M. F. Benedetto, A. Caggiano, G. Etse, Virtual elements and zero thickness interface-based approach for fracture analysis of heterogeneous materials, Computer Methods in Applied Mechanics and Engineering 338 (2018) 41–67.

[11] M. L. De Bellis, P. Wriggers, B. Hudobivnik, G. Zavarise, Virtual element formulation for isotropic damage, Finite Elements in Analysis and Design 144 (2018) 38–48.

[12] M. Lo Cascio, I. Benedetti, V. Mantič, Micro damage and cracking in fibre reinforced composites by a novel hybrid numerical technique, AIP Conference Proceedings 2309 (1) (2020) 020001. arXiv:https://aip.scitation.org/doi/pdf/10.1063/5.0033974, doi:10.1063/5.0033974.
URL https://aip.scitation.org/doi/abs/10.1063/5.0033974

[13] E. Artioli, L. B. Da Veiga, F. Dassi, Curvilinear virtual elements for 2d solid mechanics applications, Computer Methods in Applied Mechanics and Engineering 359 (2020) 112667.

[14] M. Marino, B. Hudobivnik, P. Wriggers, Computational homogenization of polycrystalline materials with the virtual element method, Computer Methods in Applied Mechanics and Engineering 355 (2019) 349 – 372. doi:https://doi.org/10.1016/j.cma.2019.06.004.
URL http://www.sciencedirect.com/science/article/pii/S0045782519303445

[15] M. L. Cascio, A. Milazzo, I. Benedetti, Virtual element method for computational homogenization of composite and heterogeneous materials, Composite Structures 232 (2020) 111523.

[16] M. Lo Cascio, A. Milazzo, I. Benedetti, Virtual element method: Micro-mechanics applications, in: Key Engineering Materials, Vol. 827, Trans Tech Publ, 2020, pp. 128–133.

[17] D. [van Huyssteen], B. Reddy, A virtual element method for isotropic hyperelasticity, Computer Methods in Applied Mechanics and Engineering 367 (2020) 113134. doi:https://doi.org/10.1016/j.cma.2020.113134.
URL http://www.sciencedirect.com/science/article/pii/S0045782520303194

[18] P. K. Banerjee, R. Butterfield, Boundary element methods in engineering science, Vol. 17, McGraw-Hill London, 1981.

[19] M. H. Aliabadi, The Boundary Element Method: applications in solids and structures., Vol. 2, John Wiley & Sons Ltd, England, 2002.

[20] I. Benedetti, M. H. Aliabadi, A three-dimensional grain boundary formulation for microstructural modeling of polycrystalline materials, Computational Materials Science 67 (2013) 249–260.

[21] L. C. Wrobel, The Boundary Element Method: applications in thermo-fluids and acoustics, Vol. 1, John Wiley & Sons Ltd, 2002.

[22] G. Sfantos, M. Aliabadi, Multi-scale boundary element modelling of material degradation and fracture, Computer Methods in Applied Mechanics and Engineering 196 (7) (2007) 1310 – 1329. doi:https://doi.org/10.1016/j.cma.2006.09.004.
URL http://www.sciencedirect.com/science/article/pii/S0045782506002891

[23] V. Gulizzi, A. Milazzo, I. Benedetti, An enhanced grain-boundary framework for computational homogenization and micro-cracking simulations of polycrystalline materials, Computational Mechanics 56 (4) (2015) 631–651. doi:10.1007/s00466-015-1192-8.

[24] I. Benedetti, M. Aliabadi, Multiscale modeling of polycrystalline materials: A boundary element approach to material degradation and fracture, Computer Methods in Applied Mechanics and Engineering 289 (2015) 429 – 453. doi:https://doi.org/10.1016/j.cma.2015.02.018.
URL http://www.sciencedirect.com/science/article/pii/S0045782515000675

[25] I. Benedetti, V. Gulizzi, V. Mallardo, A grain boundary formulation for crystal plasticity, International Journal of Plasticity 83 (2016) 202 – 224. doi:https://doi.org/10.1016/j.ijplas.2016.04.010.
URL http://www.sciencedirect.com/science/article/pii/S0749641916300596

[26] G. Geraci, M. Aliabadi, Micromechanical modelling of cohesive thermoelastic cracking in orthotropic polycrystalline materials, Computer Methods in Applied Mechanics and Engineering 339 (2018) 567 – 590. doi:https://doi.org/10.1016/j.cma.2018.05.011.
URL http://www.sciencedirect.com/science/article/pii/S0045782518302548

[27] I. Benedetti, V. Gulizzi, A grain-scale model for high-cycle fatigue degradation in polycrystalline materials, International Journal of Fatigue 116 (2018) 90 – 105. doi:https://doi.org/10.1016/j.ijfatigue.2018.06.010.
URL http://www.sciencedirect.com/science/article/pii/S0142112318302287

[28] I. Benedetti, V. Gulizzi, A. Milazzo, A microstructural model for homogenisation and cracking of piezoelectric polycrystals, Computer Methods in Applied Mechanics and Engineering 357 (2019) 112595. doi:https://doi.org/10.1016/j.cma.2019.112595.
URL http://www.sciencedirect.com/science/article/pii/S0045782519304712

[29] A. Adessina, J.-F. Barthélémy, F. Lavergne, A. B. Fraj, Effective elastic properties of materials with inclusions of complex structure, International Journal of Engineering Science 119 (2017) 1 – 15. doi:https://doi.org/10.1016/j.ijengsci.2017.03.015.
URL http://www.sciencedirect.com/science/article/pii/S0020722517304809

[30] Y. Chen, M. Aliabadi, Micromechanical modelling of the overall response of plain woven polymer matrix composites, International Journal of Engineering Science 145 (2019) 103163. doi:https://doi.org/10.1016/j.ijengsci.2019.103163.
URL http://www.sciencedirect.com/science/article/pii/S0020722519307773

[31] O. Zienkiewicz, D. Kelly, P. Bettess, The coupling of the finite element method and boundary solution procedures, International journal for numerical methods in engineering 11 (2) (1977) 355–375.

[32] T. Belytschko, H. Chang, Y. Lu, A variationally coupled finite element-boundary element method, Computers & structures 33 (1) (1989) 17–20.

[33] T. Cruse, J. Osias, Issues in merging the finite element and boundary integral equation methods, Mathematical and Computer Modelling 15 (3-5) (1991) 103–118.

[34] S. Berrone, A. Borio, C. Fidelibus, S. Pieraccini, S. Scialò, F. Vicini, Advanced computation of steady-state fluid flow in discrete fracture-matrix models: Fem–bem and vem–vem fracture-block coupling, GEM-International Journal on Geomathematics 9 (2) (2018) 377–399.

[35] F. Aurenhammer, Voronoi diagrams - a survey of a fundamental geometric data structure, ACM Comput. Surv. 23 (3) (1991) 345?405. doi:10.1145/116873.116880.
URL https://doi.org/10.1145/116873.116880

[36] D. Engwirda, Locally-optimal delaunay-refinement and optimisation-based mesh generation, Ph.D. thesis, School of Mathematics and Statistics, The University of Sydney (2004).

[37] N. Sukumar, A. Tabarraei, Conforming polygonal finite elements, International Journal for Numerical Methods in Engineering 61 (12) (2004) 2045–2066.

[38] E. Artioli, L. Beirão Da Veiga, C. Lovadina, E. Sacco, Arbitrary order 2d virtual elements for polygonal meshes: Part i, elastic problem, Computational Mechanics 60 (3) (2017) 355–377.

[39] L. Beirão da Veiga, F. Brezzi, L. D. Marini, Virtual elements for linear elasticity problems, SIAM Journal on Numerical Analysis 51 (2) (2013) 794–812.

[40] L. Beirão da Veiga, F. Brezzi, A. Cangiani, G. Manzini, L. D. Marini, A. Russo, Basic principles of virtual element methods, Mathematical Models and Methods in Applied Sciences 23 (01) (2013) 199–214.

[41] L. Kachanov, On the time of fracture under conditions of creep, Izv. AN SSSR, Otd. Tekh. Nauk,(8) (1958) 26–35.

[42] Y. N. Rabotnov, Creep rupture, in: Applied mechanics, Springer, 1969, pp. 342–349.

[43] J. Hult, Creep in continua and structures, in: Topics in applied continuum mechanics, Springer, 1974, pp. 137–155.

[44] J. Lemaitre, Local approach of fracture, Engineering Fracture Mechanics 25 (5-6) (1986) 523–537.

[45] J. C. Simo, J. Ju, Strain-and stress-based continuum damage modelsi. formulation, International journal of solids and structures 23 (7) (1987) 821–840.

[46] J. Simo, J. Ju, Strain-and stress-based continuum damage modelsii. computational aspects, International journal of solids and structures 23 (7) (1987) 841–869.

[47] J. L. Chaboche, Continuum Damage Mechanics: Part I?General Concepts, Journal of Applied Mechanics 55 (1) (1988) 59–64. arXiv:https://asmedigitalcollection.asme.org/appliedmechanics/article-pdf/55/1/59/5459827/59_1.pdf, doi:10.1115/1.3173661. URL https://doi.org/10.1115/1.3173661

[48] J. Lemaitre, J.-L. Chaboche, A. Benallal, R. Desmorat, Mécanique des matériaux solides, Vol. 2, Dunod Paris, 1985.

[49] J. Mazars, Application de la mécanique de l'endommagement au comportement non linéaire et à la rupture du béton de structure, THESE DE DOCTEUR ES SCIENCES PRESENTEE A L'UNIVERSITE PIERRE ET MARIE CURIE-PARIS 6.

[50] A. Melro, P. Camanho, F. A. Pires, S. Pinho, Micromechanical analysis of polymer composites reinforced by unidirectional fibres: Part i–constitutive modelling, International Journal of Solids and Structures 50 (11-12) (2013) 1897–1905.

[51] M. Jirásek, Nonlocal damage mechanics, Revue européenne de génie civil 11 (7-8) (2007) 993–1021.

[52] L. Beirão da Veiga, C. Lovadina, D. Mora, A virtual element method for elastic and inelastic problems on polytope meshes, Computer Methods in Applied Mechanics and Engineering 295 (2015) 327 – 346. doi:https://doi.org/10.1016/j.cma.2015.07.013.
URL http://www.sciencedirect.com/science/article/pii/S004578251500225X

[53] E. Artioli, L. Beirão Da Veiga, C. Lovadina, E. Sacco, Arbitrary order 2d virtual elements for polygonal meshes: Part ii, inelastic problem, Computational Mechanics 60 (4) (2017) 643–657.

[54] G. Pijaudier-Cabot, Z. P. Bažant, Nonlocal damage theory, Journal of engineering mechanics 113 (10) (1987) 1512–1533.

[55] M. Jirasek, Nonlocal models for damage and fracture: comparison of approaches, International Journal of Solids and Structures 35 (31-32) (1998) 4133–4145.

[56] Z. P. Bažant, M. Jirásek, Nonlocal integral formulations of plasticity and damage: survey of progress, Journal of engineering mechanics 128 (11) (2002) 1119–1149.

[57] G. Borino, B. Failla, F. Parrinello, A symmetric nonlocal damage theory, International Journal of Solids and Structures 40 (13-14) (2003) 3621–3645.

[58] M. Jirásek, M. Bauer, Numerical aspects of the crack band approach, Computers & structures 110 (2012) 60–78.

[59] C. Brebbia, The Boundary Element Method For Engineers, Pentech Press, 1984.
URL https://books.google.it/books?id=HuoeAQAAIAAJ

[60] P. Banerjee, The boundary element methods in engineering, McGraw-Hill, 1994, (pp. 177–188).

[61] P. R. Johnston, D. Elliott, A sinh transformation for evaluating nearly singular boundary element integrals, International Journal for Numerical Methods in Engineering 62 (4)

(2005) 564–578. arXiv:https://onlinelibrary.wiley.com/doi/pdf/10.1002/nme.1208, doi:https://doi.org/10.1002/nme.1208.
URL https://onlinelibrary.wiley.com/doi/abs/10.1002/nme.1208

[62] G. Xie, J. Zhang, X. Qin, G. Li, New variable transformations for evaluating nearly singular integrals in 2d boundary element method, Engineering Analysis with Boundary Elements 35 (6) (2011) 811 – 817. doi:https://doi.org/10.1016/j.enganabound.2011.01.009.
URL http://www.sciencedirect.com/science/article/pii/S0955799711000208

[63] C. Brebbia, P. Georgiou, Combination of boundary and finite elements in elastostatics, Applied Mathematical Modelling 3 (3) (1979) 212–220.

[64] L. Hong-Bao, H. Guo-Ming, H. A. Mang, P. Torzicky, A new method for the coupling of finite element and boundary element discretized subdomains of elastic bodies, Computer Methods in Applied Mechanics and Engineering 54 (2) (1986) 161–185.

[65] S. Nemat-Nasser, M. Hori, Micromechanics: overall properties of heterogeneous materials, Elsevier, 2013.

[66] T. Kanit, S. Forest, I. Galliet, V. Mounoury, D. Jeulin, Determination of the size of the representative volume element for random composites: statistical and numerical approach, International Journal of Solids and Structures 40 (13-14) (2003) 3647–3679. doi:https://doi.org/10.1016/S0020-7683(03)00143-4.
URL http://www.sciencedirect.com/science/article/pii/S0020768303001434

[67] F. Fritzen, T. Böhlke, E. Schnack, Periodic three-dimensional mesh generation for crystalline aggregates based on voronoi tessellations, Computational Mechanics 43 (5) (2009) 701–713.

[68] P. Soden, M. J. Hinton, A. Kaddour, Lamina properties, lay-up configurations and loading conditions for a range of fibre reinforced composite laminates, in: Failure Criteria in Fibre-Reinforced-Polymer Composites, Elsevier, 2004, pp. 30–51.

[69] K. Terada, M. Hori, T. Kyoya, N. Kikuchi, Simulation of the multi-scale convergence in computational homogenization approaches, International Journal of Solids and Structures 37 (16) (2000) 2285–2311.

[70] S. Swaminathan, S. Ghosh, N. Pagano, Statistically equivalent representative volume elements for unidirectional composite microstructures: Part i-without damage, Journal of Composite Materials 40 (7) (2006) 583–604.

[71] D. Trias, J. Costa, A. Turon, J. Hurtado, Determination of the critical size of a statistical representative volume element (srve) for carbon reinforced polymers, Acta materialia 54 (13) (2006) 3471–3484.

[72] I. Gitman, H. Askes, L. Sluys, Representative volume: existence and size determination, Engineering fracture mechanics 74 (16) (2007) 2518–2534.

[73] D. Łydżba, A. Różański, D. Stefaniuk, Equivalent microstructure problem: Mathematical formulation and numerical solution, International Journal of Engineering Science 123 (2018) 20 – 35. doi:https://doi.org/10.1016/j.ijengsci.2017.11.007.
URL http://www.sciencedirect.com/science/article/pii/S0020722517318980

[74] P. Karimi, A. Malyarenko, M. Ostoja-Starzewski, X. Zhang, Rve problem: Mathematical aspects and related stochastic mechanics, International Journal of Engineering Science 146 (2020) 103169. doi:https://doi.org/10.1016/j.ijengsci.2019.103169.
URL http://www.sciencedirect.com/science/article/pii/S0020722519319184

[75] R. Hill, Elastic properties of reinforced solids: Some theoretical principles, Journal of the Mechanics and Physics of Solids 11 (5) (1963) 357 – 372. doi:https://doi.org/10.1016/0022-5096(63)90036-X.
URL http://www.sciencedirect.com/science/article/pii/002250966390036X

[76] Z. Hashin, On elastic behaviour of fibre reinforced materials of arbitrary transverse phase geometry, Journal of the Mechanics and Physics of Solids 13 (3) (1965) 119 – 134. doi:https://doi.org/10.1016/0022-5096(65)90015-3.
URL http://www.sciencedirect.com/science/article/pii/0022509665900153

[77] H. Kormeling, H. Reinhardt, Determination of the fracture energy of normal concrete and epoxy modified concrete, Delft University of Technology, Report (1983) 5–83.

[78] M. Toya, A crack along the interface of a circular inclusion embedded in an infinite solid, Journal of the Mechanics and Physics of Solids 22 (5) (1974) 325–348.

[79] Z. Gao, A Circular Inclusion With Imperfect Interface: Eshelby?s Tensor and Related Problems, Journal of Applied Mechanics 62 (4) (1995) 860–866. arXiv:https://asmedigitalcollection.asme.org/appliedmechanics/article-pdf/62/4/860/5463961/860_1.pdf, doi:10.1115/1.2896012.
URL https://doi.org/10.1115/1.2896012

[80] F. París, E. Correa, V. Mantič, Kinking of transversal interface cracks between fiber and matrix, ASME Journal of Applied Mechanics 74 (4) (2007) 703–716.

[81] V. Mantič, Interface crack onset at a circular cylindrical inclusion under a remote transverse tension. application of a coupled stress and energy criterion, International journal of Solids and Structures 46 (6) (2009) 1287–1304.

[82] L. Távara, V. Mantič, E. Graciani, F. París, Bem analysis of crack onset and propagation along fiber–matrix interface under transverse tension using a linear elastic–brittle interface model, Engineering Analysis with Boundary Elements 35 (2) (2011) 207–222.

[83] I. García, M. Paggi, V. Mantič, Fiber-size effects on the onset of fiber–matrix debonding under transverse tension: a comparison between cohesive zone and finite fracture mechanics models, Engineering Fracture Mechanics 115 (2014) 96–110.

[84] M. Cid Alfaro, A. Suiker, R. De Borst, Transverse failure behavior of fiber-epoxy systems, Journal of Composite Materials 44 (12) (2010) 1493–1516.

[85] Y. Liu, Fast multipole boundary element method: theory and applications in engineering, Cambridge university press, 2009.

[86] M. Bebendorf, Hierarchical matrices, Springer, 2008.

[87] I. Benedetti, M. Aliabadi, G. Dav, A fast 3d dual boundary element method based on hierarchical matrices, International Journal of Solids and Structures 45 (7) (2008) 2355 – 2376. doi:https://doi.org/10.1016/j.ijsolstr.2007.11.018.
URL http://www.sciencedirect.com/science/article/pii/S0020768307005008

[88] I. Benedetti, A. Milazzo, M. H. Aliabadi, A fast dual boundary element method for 3d anisotropic crack problems, International Journal for Numerical Methods in Engineering

80 (10) (2009) 1356–1378. arXiv:https://onlinelibrary.wiley.com/doi/pdf/10.1002/nme.2666, doi:10.1002/nme.2666.
URL https://onlinelibrary.wiley.com/doi/abs/10.1002/nme.2666

[89] I. Benedetti, M. H. Aliabadi, A fast hierarchical dual boundary element method for three-dimensional elastodynamic crack problems, International Journal for Numerical Methods in Engineering 84 (9) (2010) 1038–1067. arXiv:https://onlinelibrary.wiley.com/doi/pdf/10.1002/nme.2929, doi:10.1002/nme.2929.
URL https://onlinelibrary.wiley.com/doi/abs/10.1002/nme.2929

[90] L. Gray, E. Lutz, On the treatment of corners in the boundary element method, Journal of Computational and Applied Mathematics 32 (3) (1990) 369–386. doi:https://doi.org/10.1016/0377-0427(90)90043-Y.
URL https://www.sciencedirect.com/science/article/pii/037704279090043Y

[91] I. Benedetti, M. H. Aliabadi, A three-dimensional cohesive-frictional grain-boundary micromechanical model for intergranular degradation and failure in polycrystalline materials, Computer Methods in Applied Mechanics and Engineering 265 (2013) 36–62.

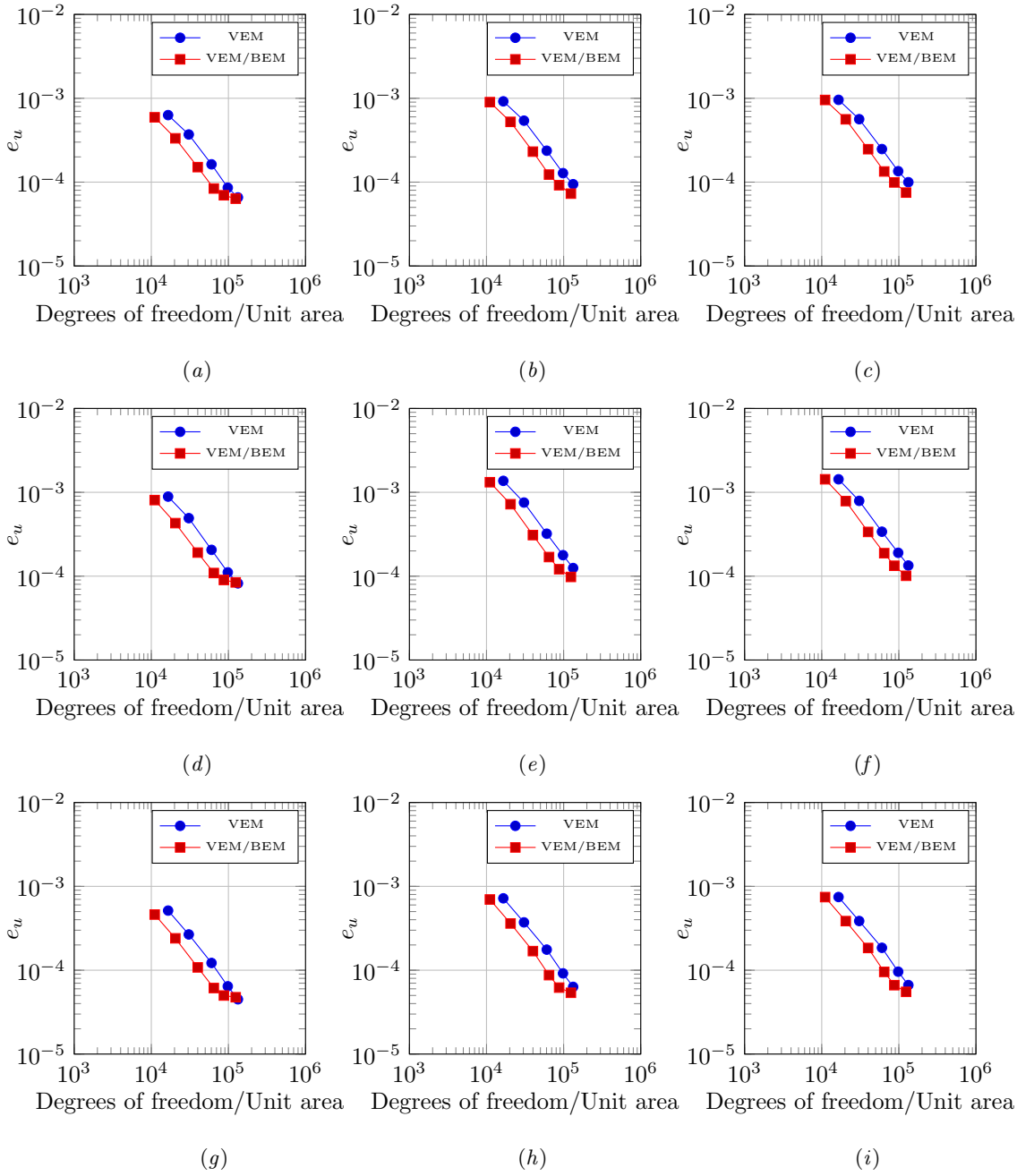

Fig. 8. Comparison between the convergence of the VE solutions and that of the hybrid VE-BE solution in terms of displacements. The rows of the plots grid correspond to the different considered boundary conditions, namely BC_x (a,b,c), BC_y (d,e,f), BC_{xy} (g,h,i). The columns correspond to the different materials, i.e. M10 (a,d,g), M100 (b,e,h), M1000 (c,f,i).

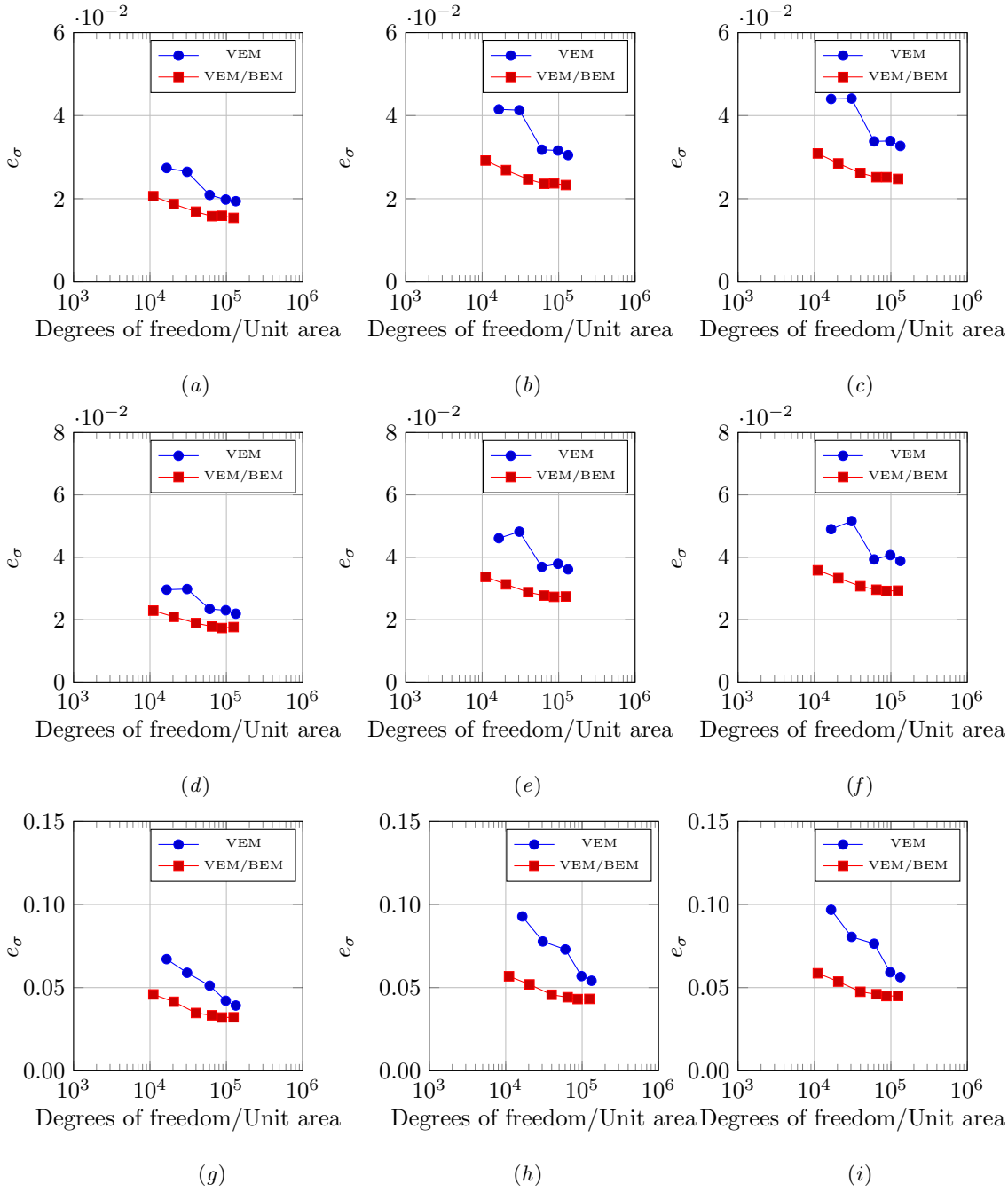

Fig. 9. Comparison between the convergence of the VE solutions and that of the hybrid VE-BE solution in terms of stresses. The rows of the plots grid correspond to the different considered boundary conditions, namely BC_x (a,b,c), BC_y (d,e,f), BC_{xy} (g,h,i). The columns correspond to the different materials, i.e. M10 (a,d,g), M100 (b,e,h), M1000 (c,f,i).

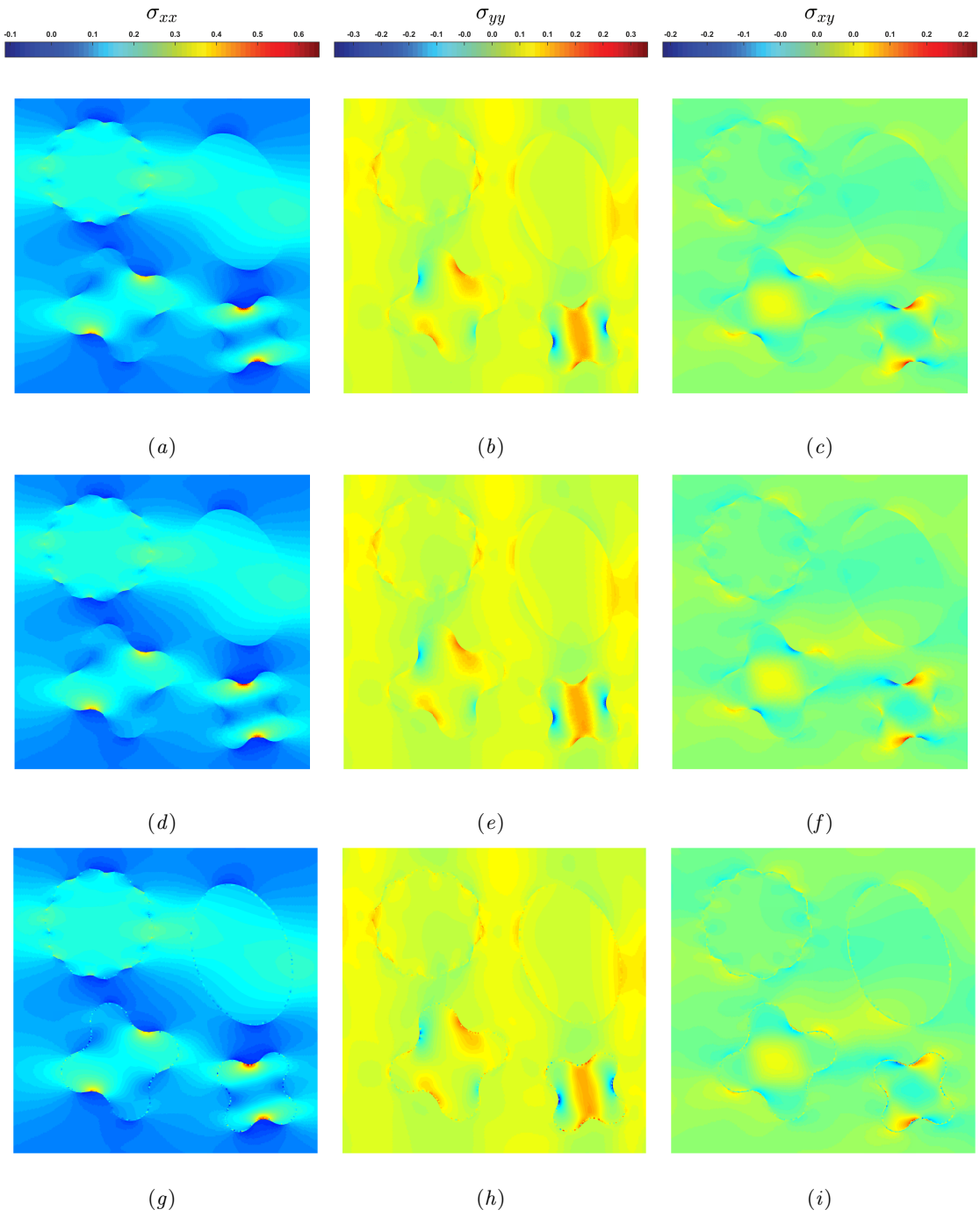

Fig. 10. From left to right, plot of stress components σ_{xx}, σ_{yy} and σ_{xy} [GPa] corresponding to an enforced uniaxial strain $\bar{\epsilon}_{xx} = 0.05$ computed by using (a,b,c) ~~the~~ FEM, (d,e,f) ~~the~~ VEM and (g,h,i) the hybrid VEM-BEM scheme. The comparison highlights remarkable agreement among the three different solutions.

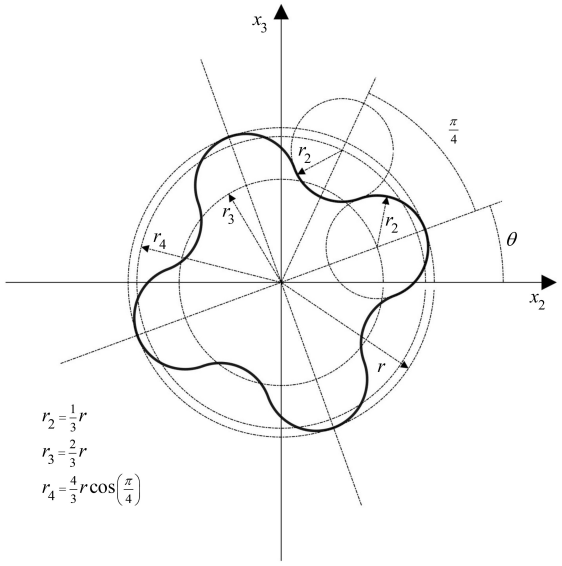

Fig. 11. Geometry of the transversal section of the inclusions randomly placed within the analysed unit cells.

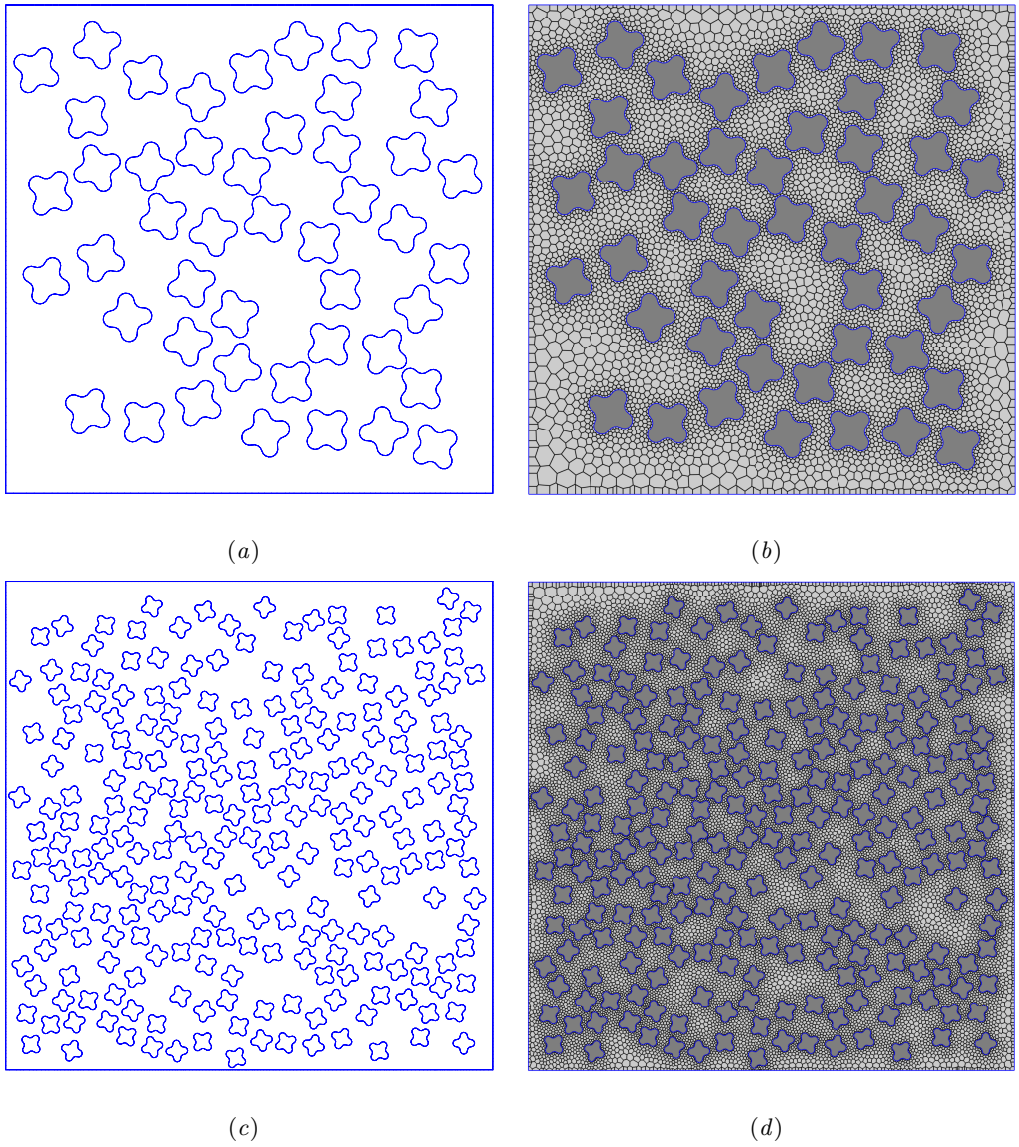

Fig. 12. Examples of unit cells employed in the computational homogenization tests: random geometries obtained by setting $V_f = 0.25$ and *a)* $\delta = 20$ *c)* $\delta = 45$; *b,d)* meshes employed for the VE-BE analyses.

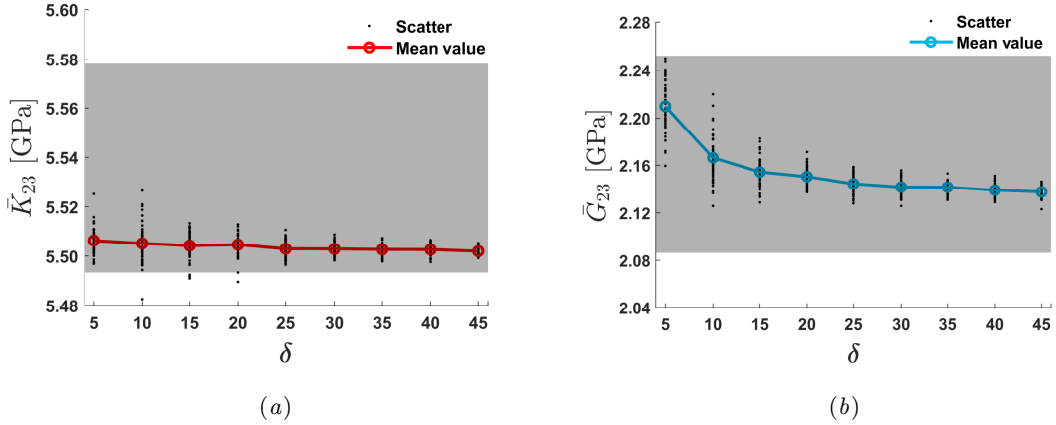

Fig. 13. Apparent transverse elastic properties $\bar{K}_{23}$ and $\bar{G}_{23}$ as a function of δ for $V_f = 0.25$ as computed using the hybrid virtual-boundary element technique. The Hashin-Hill bounds for the considered composite are identified by the grey area.

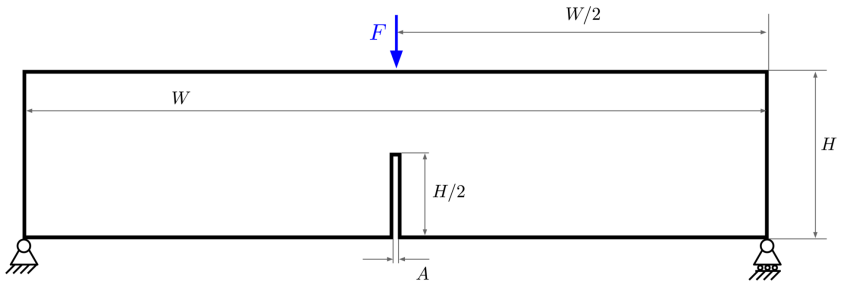

Fig. 14. Geometry and boundary conditions of the three-point bending test.

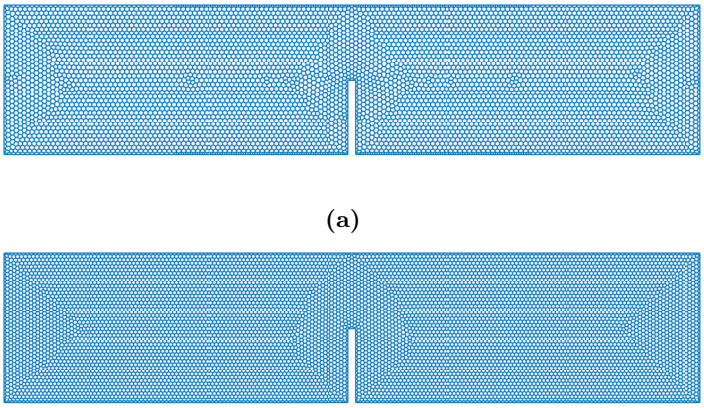

Fig. 15. Polygonal meshes used in the numerical simulation of the three-point bending test: (a) mesh V1, (b) mesh V2.

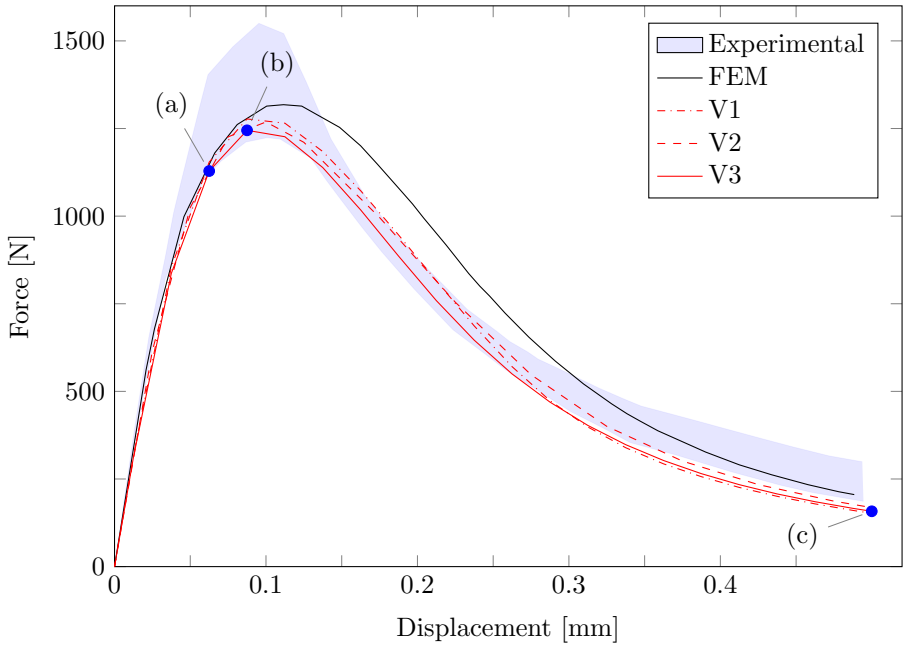

Fig. 16. Force-displacement diagram for the three-point bending test. Comparison between the virtual element discretisations, the reference FEM solution in Ref.[51] and experimental data in Ref.[77].

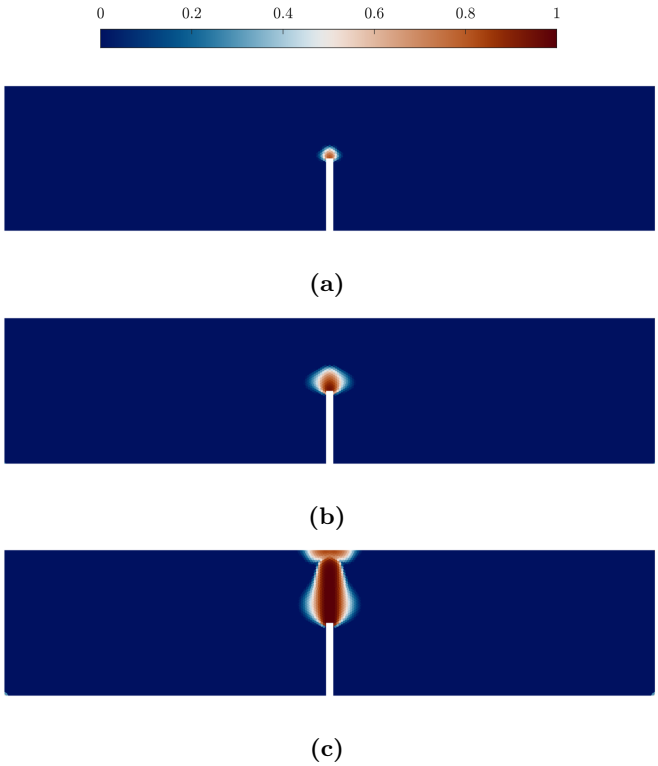

Fig. 17. Damage profile evolution for the three-point bending test (mesh V3).

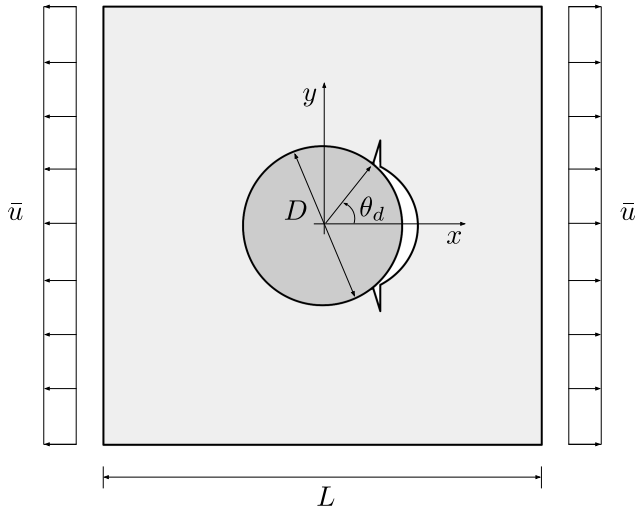

Fig. 18. Geometry and boundary conditions of the composite unit cell containing a circular fibre partially debonded from the matrix.

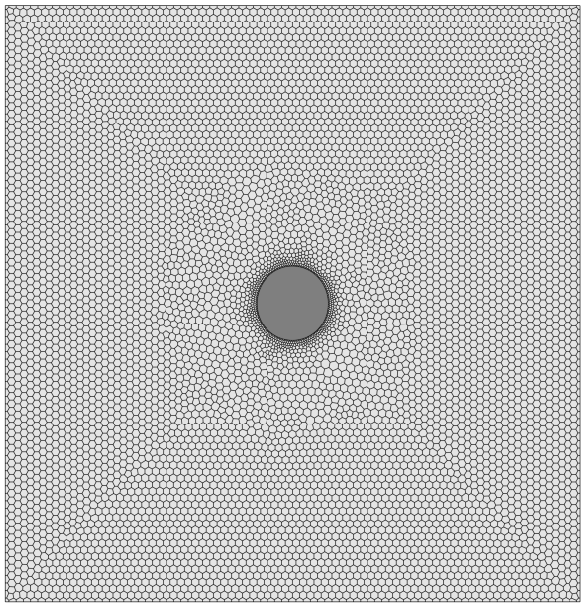

Fig. 19. The mesh adopted to simulate the transverse failure behaviour of a composite unit cell with partial debonding.

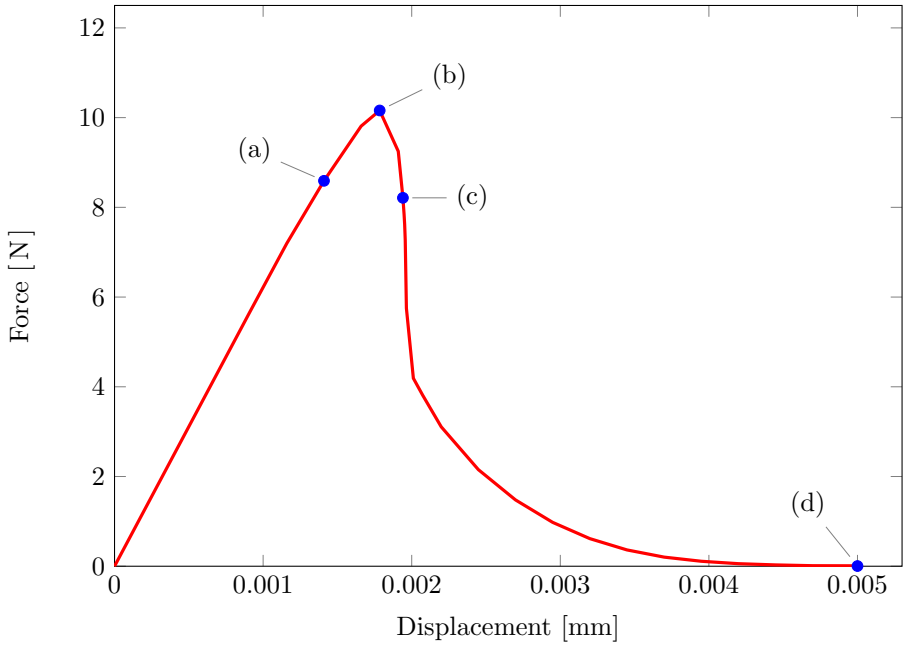

Fig. 20. Force-displacement diagram for the composite unit cell test under tensile loading.

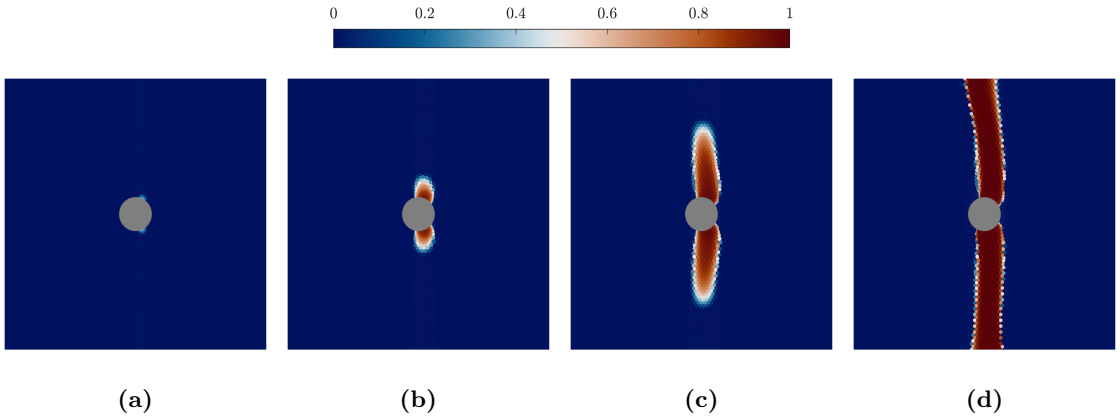

Fig. 21. Damage profile evolution for the composite unit cell under tensile loading.